

## Response to reviewer comments

J. Vira and co-authors

We thank both referees for the extensive reviews. In the following we will address the comments of reviewer #1 and the specific comments of reviewer #2. The general comment of reviewer #2 has been addressed in our response on 13 December 2016.

The main changes in the revised manuscript is extending experiments with synthetic data in Section 4 to cover assimilation of simulated plume height retrievals, and presenting a comparison between the simulated SO<sub>2</sub> profiles and the lidar data from the CALIOP instrument. These major revisions are discussed in more detail in our response to reviewer #1.

Due to the volume of new material, we have removed the discussions of two minor items present in the original submission. The omissions are Figure 5 and the related discussion (additional experiments with randomly generated source terms), and Figure 10 and the related discussion (inversion with a simplified observation error covariance matrix).

The figures for Eyjafjallajökull have been rearranged as part of the comparisons for total columns are now presented together with the CALIOP data. Figures comparing the simulated total columns and plume heights with the IASI data for all days are included in a supplement.

The manuscript with changes highlighted is attached to this pdf.

*The reviewer comments are presented with a blue italic font.*

## Response to comments by reviewer #1

We thank the referee for a thorough and detailed review. In order to address the main concerns raised by the referee, we have introduced the following major revisions to the manuscript:

1. The experiments with synthetic observations are extended to cover the case with assimilation of simulated plume height retrievals. The results are consistent with those obtained for the Eyjafjallajökull eruption. Assimilation of plume height retrievals results in a more accurate source term (in the sense of RMS error), although the difference is small for some of the assumed source terms. However, the experiment also confirms that assimilation of plume heights may have negative impact on the estimated total emission.
2. The results for Eyjafjallajökull are evaluated using profile data from the CALIOP instrument, and a detailed comparisons between the estimated injection height, the retrieved SO<sub>2</sub> plume heights, and the radar observations of plume top are presented. The comparisons show consistently that the results with and without assimilation of plume heights are largely similar but the vertical distribution of the emissions especially on 6-9 May is improved by assimilation of plume height retrievals. For the other times, the injection height is mostly consistent with the data regardless whether the plume heights are assimilated or not.

Ideally the results for total columns should be compared with independent satellite data. However, as noted in earlier studies about Eyjafjallajökull (Boichu et al., 2013; Flemming and Inness, 2013), this is unlikely to lead into useful conclusions due to the large differences between satellite products. For this reason, we have instead focused on the vertical distribution which we consider to be the most interesting of aspect of the present study.

*In the current version of the manuscript, it remains unclear what the benefit of the assimilation of the plume height is. Given the overall uncertainty and judging from the pictures, it seems that the plume height assimilation does not lead to an improvement. If this is the case it should be mentioned more clearly.*

We believe that the revised manuscript gives a more accurate and detailed picture of impact of assimilating the plume height. However, we hesitate to declare one inversion better than other, because drawing such a conclusion would require three-dimensional observational data that do not exist. The possible benefits of assimilating the plume height in addition to total column cannot be evaluated based on their impact on the simulated total columns or the total emission, because these quantities are fit optimally when only total column data are assimilated.

Based on the experiments with synthetic data and the comparison to vertically resolved observations for Eyjafjallajökull, it seems reasonable to conclude that assimilating the plume height retrieval has a positive impact on the vertical distribution, even if the effect is small when taken over the whole eruption. Similarly, the experiments indicate that the impact on total columns and total emission is negative. Whether one of these effects outweighs the other depends on the application.

*The presented 4D-VAR approach does not take into account correctly the error statistics of the assimilating model as no model error co-variances are considered. This seems a simplification which should be better justified.*

We agree that the treatment of model errors is not ideal, however, as pointed out in the initial response to reviewer #2, the problem is challenging and we are not aware of any inversion study that would have addressed this aspect without simplifications.

Inclusion of the model errors into the R-matrix is necessary because the inversion is performed in a single, long assimilation window. As discussed in the revised manuscript, it would be in principle possible to set up the inversion as a sequence of shorter assimilation windows as done by Elbern et al. (2007) in context of air quality forecasting. However, when the primary interest is to estimate an emission source, this approach becomes more complicated because of two opposing requirements. The first requirement is that the assimilation window needs to be short enough so that the model errors arising within the assimilation window are not significant – this is the basic assumption of the currently used strong-constraint assimilation methods. The second requirement is that the assimilation window should be long enough to effectively constrain the emission. Shorter assimilation windows may be useful for constraining constant or slowly varying emissions, but such assumptions would not hold for volcanic emissions.

So far, the majority of studies on inverse modelling of atmospheric emissions have emphasized the second aspect and used long assimilation windows. This includes the inversions for volcanic emissions (Boichu et al., 2013; Kristiansen et al., 2010; Lu et al., 2016; Stohl et al., 2011), where the inversion is done for the entire eruption at once, but also inversions for other trace gas emissions (e.g. Meirink et al. 2008; Müller and Stavrakou, 2005) or for inverse modelling of accidental radioactive releases (e.g. Winiarek et al., 2014). An advantage of the long assimilation window without explicit model errors is that the no unphysical sources or sinks appear due to the assimilation, and the mass budget of the simulation remains closed. While this does not imply that the long-window approach is superior to the other options, a comparison of its advantages and disadvantages is outside the scope of the current paper.

*Also, it seems that the SILAM model did not consider a chemical loss for SO<sub>2</sub>, which – if this was the case – would be an unnecessary simplification of the model.*

As noted on L76 in Section 2.1 (Dispersion model), the model does include chemical removal of SO<sub>2</sub>.

*L 17: Clarify “vertical centre of mass” and “first moment”*

Done.

*L 20: Mention the relation of regularization with the a-priori estimate here.*

Done.

*L 50: Discuss the issue of the “single value” plume height retrieval and the observed complex SO<sub>2</sub> profiles and the resulting challenges for the assimilation.*

A discussion has been added onwards of L65.

*L 64: Clarify the differences between the “inversion type studies” using Lagrangian models, the 4D-VAR approach for the assimilation of only concentrations and the inclusion of the emission term in these 4D-VAR systems.*

Additional discussion has been added on lines 70-76.

*L 91: Say what the data set entails: TC and plume heights retrievals*

“The algorithm and the dataset are explained in more detail by Carboni et al. (2012)” has been changed into “The algorithm and the IASI SO<sub>2</sub> dataset (column amount and altitude) are explained in more detail by Carboni et al. (2012)”.

*L 99: What is the effective plume height?*

The effective altitude is the altitude of the mean of the Gaussian distribution that fits the measurements. We called it “effective” because we assume one SO<sub>2</sub> layer with a Gaussian profile. To clarify we have changed the text: “The scheme determines the column amount and effective altitude of the SO<sub>2</sub> plume” is changed into: “The scheme determines the column amount and the altitude (mean of Gaussian distribution) of the SO<sub>2</sub> plume”.

*L 103: If this is the ash plume height - why the ash plume height?*

This is the altitude of the SO<sub>2</sub> plume, not the ash plume; to avoid misunderstanding we have changed the text:

“The altitude retrieved for the Eyjafjallajökull eruption plume”

into

“The SO<sub>2</sub> altitude retrieved for the Eyjafjallajökull eruption”.

*L 155: What are inversion experiments. Please clarify the use of the terms “data assimilation” and “inversion” throughout the paper (see L64).*

The present study is best described as a (source term) inversion similarly to the studies cited in our response to the comment regarding the 4D-Var method. We nevertheless use the word “assimilate” in reference to the action of an observation operator (as in “to assimilate plume height retrievals”), since this is both intuitive and consistent with existing literature on inverse modelling.

*L 122: The “inversion” with simulated observations is discussed before the Eyjafjallajökull case. So please also mention them here before.*

Done.

*L 128: Is the conversion of SO<sub>2</sub> to SO<sub>4</sub> considered in the study?*

Yes, as indicated above. A remark has been added also here.

*L 140: Please discuss that the standard 4D-VAR approach would include the model error in form of the background error covariance matrix.*

We have included a discussion on model errors and possible ways to handle them.

*L 146: Spell out L-BFGS-B*

Done.

*L 156: Define also  $y$  and  $m_{ij}$*

Done.

*L 160: Provide the formulae for centre of mass and 1st moment of mass*

Done.

*L 175: It is not clear if  $R$  also contains the error of the plume height retrieval. Is this error also provided and used?*

The plume height retrieval error is provided and used. The corresponding text has been added.

*L 204: This is not surprising given that the model/background error is ignored in equation (2)*

*L 209: Having only a diagonal model error covariance ignores the fact that the model advects the tracer.*

We refer to our response above regarding the 4D-Var formulation.

*L 219: Provide reference or explanation for the Tikhonov regularisation*

References have been added.

*L 252: Please describe the setting of the synthetic experiment better. What was period, region and meteorological data? Is only the emission term synthetic? What are the synthetic observations?*

The section has been rewritten for more clarity. With synthetic observations we refer to simulated observations and observation errors. In addition, we have simplified the section by omitting the additional experiment (Fig. 5) with randomly generated source terms.

*L 315: What is meant by “overall need”? Why is there an assumption about the source term? I thought regularizations is introduced to avoid an prior assumption for the source term? From which of the above are these generalisations deduced?*

By the need for regularisation we meant that the sensitivity to under-regularisation varied between the assumed sources. However, we agree that this was formulated unclearly, and the paragraph has been rephrased.

*L 316: In which of the experiments there was no model error? Please clarify. Perhaps a table of all the synthetic experiments would be useful.*

We have clarified that model error was present in all experiments except for creating Fig. 2.

*L 320: Say exactly which type of experiment you refer to*

Done.

*L 322: Motivate this choice of the 9th and 13th iterate better. I thought that the L-curve needs to be examined for every case specifically.*

The iterates were chosen according to the algorithm described on lines 364-366 in the revised manuscript. We also examined the L-curves visually but kept the points chosen by the algorithm. The L-curves are provided in supplementary information.

*L 324: Over plotting the observed ash plume height in Figure 7 is not really instructive. You should try to plot the time series of the averaged emission centre from the two inversions together with the retrieved plume height (see Figure 13) in the vicinity of the volcano. This would show how much the plume height observations in the whole domain constrain the injection profile over the volcano. The observed ash plume height, which is basically the lower border of the ash plume, is less instructive. Consider showing the difference between the two inversions in Figure 7b.*

As stated in Arason et al. (2011), the radar time series actually represent the upper border of the ash plume. While we agree that comparing the radar data with the inversion results is somewhat ambiguous, we have decided to keep the comparison, since the radar data provide an independent dataset evaluating the estimated injection height. However, we have also added a chart showing the comparison of the emission centre of mass with plume height retrievals averaged within 50 and 500 km radiuses from the volcano. We hope that Fig. 8 also exposes the differences between the inversion results in Fig. 7.

*L 328: Stating the differences between the two inversions is not enough (see my general remark). Please say which of the two inversions is better. If this is not possible, say more clearly that this is the case.*

Please see our response to the general remark.

*L 337: Please discuss in more detail, why the total emission change despite the fact that the assimilated total columns are the same.*

We have added (L562 onwards) a discussion regarding effects of the plume height assimilation on the total emission.

The total emission changes because when only total columns are assimilated, the inversion has more degrees of freedom to match the observed horizontal distribution. When a vertical constraint is added, the simulated total columns must change unless the model describes the real transport perfectly, which is not a realistic assumption. To give a concrete example, in Fig. 13 in the revised manuscript, the TC-only run appears to fit better the total column data between 50° and 54° N, shown in the lower panel with the line plots. However, the comparison with IASI and CALIOP data shows that this corresponds to an unrealistic vertical distribution. As a consequence, the TC+CM run agrees worse with the total column, but is quite likely to agree better with the true, three-dimensional distribution.

The synthetic experiments indicate that the TC+CM inversions tend to have a low bias for total mass, which is consistent with the results for Eyjafjallajökull. The likely reason is the regularisation, which among different emissions with similar likelihood prefers the one with lowest squared sum. Whether a different cost function would avoid the negative effect on total emission is a question for a future study.

*L 341: A plot of the difference with the base case would be clearer.*

*L 343: Check language "as spread as"*

*L 344: Again, it needs to be shown, that the results shown in Figure 10 are better or worse than the ones from Figure 7 before any conclusion can be drawn*

Due to the volume of new material added, and since this aspect is peripheral to the main discussion, we have omitted Fig. 10 and the associated text from the revised manuscript.

*L 349: In line 337 you say it is about 10%. Why is this the case? Were the observations errors different for the assimilated TC in the two cases? The TC and the plume height retrievals are not independent*

We rewritten the text for better self-consistency. The same observation errors were used in both experiments. The correlation between TC and plume height retrieval errors is taken into account as indicated now more clearly in Section 3.2.

*L 350: Please provide more evidence and discussion.*

More evidence (especially Fig. 8) and discussion has been added.

*L 355: I find it actually quite interesting that the additional assimilation of the plume height has so little influence.*

*L 357: Again, this is no proof that one inversion is better*

A more detailed discussion about the changes and similarities between the results has been added.

*L 366: The differences between GOME-2 and IASI plume height retrievals should be discussed in more detail. The explanation is too short.*

We mention the GOME-2 retrievals, since they are one of the few published observations on SO<sub>2</sub> plume height. As indicated, neither our data nor inverse modelling reproduces the GOME-2 plume height, but investigating the reasons for this would require a detailed comparison of the satellite products and the retrieval algorithms.

*L 366 and L 370: Compare your results for both the injection height and the SO<sub>2</sub> mass with the results published in the literature, for example Boichu et al. 2013, Flemming and Inness, 2013. This would be an important result and should be mentioned in the conclusion or abstract.*

Comparisons with Boichu et al. (2013), Flemming and Inness (2013) and Stohl et al. (2011) have been added.

*L 376: Which other studies? Provide references.*

References (Boichu et al., 2013; Seibert et al., 2011) have been added.

*L 380: This is all a bit unspecific. Please quantify the identified noise and how this could relate to the results from the 2010 case study.*

The section has been revised based on the new results using synthetic plume height observations in Section 4.

*L 390: 1000 days wall clock time or simulated days? How long does it need on a typical high performance computer architecture? What are the options for the parallelism of the application.*

The 1000 days are simulated days. We have added a discussion about the required wall clock time and the options for parallelisation in each case.

*L 400: It think it is fair to say that the assimilation of the plume height only had a small influence on the results. Also, the paper provides not enough evidence that one option is better than the other.*

We agree that the difference is mostly minor. We have expanded the Conclusions section to cover both similarities and differences between the inversions as well as the impacts on both vertical distribution and total mass.

## Response to specific comments by reviewer #2

This response extends our earlier response posted on 13 December 2016 and addresses the specific remarks by reviewer #2.

*The reviewer comments are presented with a blue italic font.*

*There is a systematic confusion between “plume height” and (height of) “centre of mass”. Both quantities seem interchangeable, so I would expect that this was described in a previous paper about the retrieval scheme. This should still be explained with proper references in section 2.2, with much more attention paid to the exact term used throughout the text (including title and abstract). Even if this was published already, consider adding a line plot in section 2.2 to compare the retrieved centre of mass with the plume height observed by radar and cameras (i.e. white dots and barely visible grey dots in figure 7). Note also that such a comparison directly above Eyjafjallajökull would still not be convincing for the downstream plume, where a multi-layered distribution probably happened.*

The term “plume height retrieval” is used previous literature (Carboni et al., 2016, 2012; Rix et al., 2012), where it is interpreted as the midpoint of some parametric representation of the vertical profile. Since our observation operator does not assume a specific shape of the profile, it is more accurately described as an observation operator for the centre of mass (or rather, the vertical first moment of mass). However, since this definition is rather technical we prefer to use the term plume height retrieval except in cases where the distinction is essential.

We have added to the introduction a remark regarding the usage of “plume height” and “centre of mass” in the revised manuscript. The manuscript now uses “plume height” in all non-technical contexts.

The revised manuscript includes a comparison between the simulated emission, the IASI retrievals and the plume top observations, and also comparisons of the simulated SO<sub>2</sub> concentration with the CALIOP profiles and collocated IASI retrievals.

*What is the width of the Gaussian distribution assumed by the retrieval algorithm? The observation operator does not take into account this Gaussian shape. We are in a case where the vertical resolution leading to the simulated observation is much, much finer than the “vertical resolution” of the observation itself so this looks like a major oversight - especially in a context where Averaging Kernels were not taken into account. In order to simulate the observations correctly, the observation operator should first fit the modelled profile with a Gaussian shape before applying equation (4). Of course this should also be included in the adjoint of the observation operator...*

The width of the Gaussian used in IASI forward model is 100 mb. The retrievals were also tested assuming different widths (50 and 10 mb), which gave results consistent with each other within the error bars.

The observation operator is based on the assumption that observations of the first moment of mass and the total column and the corresponding error covariance matrix are available. The retrievals (after application of the transformation described in Section 3.2) are consistent with this assumption, and the variability which is taken into account in the error estimates should not be included into the observation operator. Evaluating the centre of mass does not depend strongly on the model resolution.

*The sentence on lines 134-135 is extremely problematic as it seems to show a fundamental misunderstanding about assimilation theory: “Finally, the vector  $y$  of observations is given by the possibly*

*non-linear observation operator  $H$  as  $y=H(x)+\epsilon$  where  $\epsilon$  denotes the observation error."  $H(x)$  is the model state in observation space.  $y-H(x)$  is the observation departure. Here  $\epsilon$  does not denote only the observation error but all possible errors, including the model and representativity errors. Most importantly,  $y$  is not "given" by  $H$ , it is simulated by  $H$ ! This awful confusion continues in equation (3) which does not provide  $y$  but the (total component of)  $H(x)$ .*

The sentence has been rephrased.

*It appears from lines 307-312 that the assimilation algorithm can use both the algebraic solution with explicit computation of HM matrix, and the 4D-Var approach. This should be clearly explained in section 3.1. I assume that Vira and Sofiev (2012) provided all necessary details about this 4D-Var implementation and its adjoint model (e.g., was it generated automatically or manually? Is it as detailed as the forward model? How was it verified?). If that is the case, an additional reference and a few words may suffice. But if that was not the case, or if the 4D-Var implementation changed a lot (beyond the developments described in sections 3.2 and 3.3), then this should be fully described (since appropriate for the GMD journal).*

The adjoint model is same as in Vira and Sofiev, (2012). The difference is that in the 2012 study the emission adjustment was multiplicative, horizontally variable but vertically constant, while in the current study, the adjustment is additive and vertically variable but confined to a single column. This corresponds to a different summation of the adjoint variable when evaluating the gradient, but the adjoint code does not need to be changed. A remark has been added to the revised manuscript.

## References

- Arason, P., Petersen, G.N., Bjornsson, H., 2011. Observations of the altitude of the volcanic plume during the eruption of Eyjafjallajökull, April–May 2010. *Earth Syst. Sci. Data* 3, 9–17. doi:10.5194/essd-3-9-2011
- Boichu, M., Menut, L., Khvorostyanov, D., Clarisse, L., Clerbaux, C., Turquety, S., Coheur, P.-F., 2013. Inverting for volcanic SO<sub>2</sub> flux at high temporal resolution using spaceborne plume imagery and chemistry-transport modelling: the 2010 Eyjafjallajökull eruption case study. *Atmos. Chem. Phys.* 13, 8569–8584. doi:10.5194/acp-13-8569-2013
- Carboni, E., Grainger, R., Walker, J., Dudhia, a., Siddans, R., 2012. A new scheme for sulphur dioxide retrieval from IASI measurements: application to the Eyjafjallajökull eruption of April and May 2010. *Atmos. Chem. Phys.* 12, 11417–11434. doi:10.5194/acp-12-11417-2012
- Carboni, E., Grainger, R.G., Mather, T.A., Pyle, D.M., Thomas, G., Siddans, R., Smith, A., Dudhia, A., Koukouli, M.L., Balis, D., 2016. The vertical distribution of volcanic SO<sub>2</sub> plumes measured by IASI. *Atmos. Chem. Phys.* 16, 4343–4367. doi:doi:10.5194/acp-16-4343-2016
- Elbern, H., Strunk, A., Schmidt, H., Talagrand, O., 2007. Emission rate and chemical state estimation by 4-dimensional variational inversion. *Atmos. Chem. Phys.* 7, 3749–3769. doi:10.5194/acpd-7-1725-2007
- Flemming, J., Inness, A., 2013. Volcanic sulfur dioxide plume forecasts based on UV-satellite retrievals for the 2011 Grímsvötn and the 2010 Eyjafjallajökull eruption. *J. Geophys. Res. Atmos.* 118. doi:10.1002/jgrd.50753
- Kristiansen, N.I., Stohl, A., Prata, A.J., Richter, A., Eckhardt, S., Seibert, P., Hoffmann, A., Ritter, C., Bitar, L., Duck, T.J., Stebel, K., 2010. Remote sensing and inverse transport modeling of the Kasatochi eruption sulfur dioxide cloud. *J. Geophys. Res.* 115, 1–18. doi:10.1029/2009JD013286
- Lu, S., Lin, H.X., Heemink, A.W., Fu, G., Segers, A.J., 2016. Estimation of Volcanic Ash Emissions Using Trajectory-Based 4D-Var Data Assimilation. *Mon. Weather Rev.* 144, 575–589. doi:10.1175/MWR-D-15-0194.1



- Meirink, J.F., Bergamaschi, P., Krol, M.C., 2008. Four-dimensional variational data assimilation for inverse modelling of atmospheric methane emissions: method and comparison with synthesis inversion. *Atmos. Chem. Phys.* 8, 6341–6353. doi:10.5194/acpd-8-12023-2008
- Müller, J.F., Stavrou, T., 2005. Inversion of CO and NO<sub>x</sub> emissions using the adjoint of the IMAGES model. *Atmos. Chem. Phys.* 5, 1157–1186. doi:10.5194/acp-5-1157-2005
- Rix, M., Valks, P., Hao, N., Loyola, D., Schlager, H., Huntrieser, H., Flemming, J., Koehler, U., Schumann, U., Inness, A., 2012. Volcanic SO<sub>2</sub>, BrO and plume height estimations using GOME-2 satellite measurements during the eruption of Eyjafjallajökull in May 2010. *J. Geophys. Res. Atmos.* 117. doi:10.1029/2011JD016718
- Seibert, P., Kristiansen, N.I., Richter, A., Eckhardt, S., Prata, A.J., Stohl, A., 2011. Uncertainties in the inverse modelling of sulphur dioxide eruption profiles. *Geomatics, Nat. Hazards Risk* 2, 201–216. doi:10.1080/19475705.2011.590533
- Stohl, A., Prata, A.J., Eckhardt, S., Clarisse, L., Durant, A., Henne, S., Kristiansen, N.I., Minikin, A., Schumann, U., Seibert, P., Stebel, K., Thomas, H.E., Thorsteinsson, T., Tørseth, K., Weinzierl, B., 2011. Determination of time- and height-resolved volcanic ash emissions and their use for quantitative ash dispersion modeling: the 2010 Eyjafjallajökull eruption. *Atmos. Chem. Phys.* 11, 4333–4351. doi:10.5194/acp-11-4333-2011
- Vira, J., Sofiev, M., 2012. On variational data assimilation for estimating the model initial conditions and emission fluxes for short-term forecasting of SO<sub>x</sub> concentrations. *Atmos. Environ.* 46, 318–328. doi:10.1016/j.atmosenv.2011.09.066
- Winiarek, V., Bocquet, M., Duhanyan, N., Roustan, Y., Saunier, O., Mathieu, A., 2014. Estimation of the caesium-137 source term from the Fukushima Daiichi nuclear power plant using a consistent joint assimilation of air concentration and deposition observations. *Atmos. Environ.* 82, 268–279. doi:10.1016/j.atmosenv.2013.10.017

# Variational assimilation of IASI ~~SO<sub>2</sub>~~SO<sub>2</sub> plume height and total-column retrievals in the 2010 eruption of Eyjafjallajökull using the SILAM v5.3 chemistry transport model

Julius Vira<sup>1</sup>, Elisa Carboni<sup>2</sup>, Roy G. ~~Grainger~~<sup>3</sup>Grainger<sup>2</sup>, Mikhail Sofiev<sup>1</sup>

<sup>1</sup> Finnish Meteorological Institute, Erik Palménin aukio 1, FI-00560 Helsinki, Finland

<sup>2</sup> COMET, Atmospheric, Oceanic and Planetary Physics, University of Oxford, Parks Road, Oxford, OX1 3PU, U.K.

~~<sup>3</sup> National Centre for Earth Observation, Atmospheric, Oceanic and Planetary Physics, University of Oxford, Parks Road, Oxford OX1 3PU, U.K.~~

Correspondence to: J. Vira, julius.vira@fmi.fi

## Abstract

This study focuses on two new aspects on inverse modelling of volcanic emissions. First, we derive an observation operator for satellite retrievals of plume height, and second, we solve the inverse problem using an algorithm based on the 4D-Var data assimilation method. The approach is first tested in a twin experiment with simulated observations and further evaluated/demonstrated by assimilating IASI ~~SO<sub>2</sub>~~SO<sub>2</sub> plume height and total column retrievals in a source term inversion for the 2010 eruption of Eyjafjallajökull. The inversion resulted in temporal and vertical reconstruction of the ~~SO<sub>2</sub>~~SO<sub>2</sub> emissions during the 1-201 May, 2010 with formal vertical and temporal resolutions of 500 m and 12 hours.

The plume height observation operator is based on simultaneous assimilation of the plume height and total column retrievals. The plume height is taken to represent the vertical centre of mass, which is transformed into the first moment of mass (centre of mass times total mass). This makes the observation operator linear and simple to implement. The necessary modifications to the observation error covariance matrix are derived.

Regularisation by truncated iteration is investigated as a simple and efficient regularisation method for the 4D-Var based inversion. In the twin experiments, the truncated iteration was found to perform similarly to the commonly used Tikhonov regularisation, which in turn is equivalent to a Gaussian a priori source term. However, the truncated iteration allows the level of regularisation to be determined a posteriori without repeating the inversion.

In the twin experiments, assimilating the plume height retrievals resulted in 5-20% improvement in root mean squared error but simultaneously introduced a 10-20% low bias on the total emission depending on assumed emission profile. The results are consistent with those obtained with real data. For Eyjafjallajökull, the comparison between results with and without assimilation of plume height retrievals shows that the estimated injection height was mostly constrained by the inversion even using only total column retrievals. However, comparison with the profile observations from the CALIOP instrument showed that assimilating the plume height retrievals improved the vertical distribution during episodes when the estimated injection height was not otherwise not sufficiently constrained.

Formatted: Finnish

Formatted: Not Highlight

32 Regularisation by truncated iteration is investigated as a simple and efficient regularisation method for the 4D-Var based  
33 inversion. In an experiment with synthetic observations, the truncated iteration was found to perform similarly to the  
34 commonly used Tikhonov regularisation. However, the truncated iteration allows the amount of regularisation to be varied a  
35 posteriori, without repeating the inversion. For inverting the Eyjafjallajökull  $\text{SO}_2$  emission at the temporal and vertical  
36 resolution used in this study, the 4D-Var method required about 70% less computational effort than commonly used methods  
37 based on performing a separate model simulation for each degree of freedom in the estimated source term.

38 Compared to the inversion using only total column retrievals, assimilating the plume height resulted in a vertical emission  
39 profile more closely matching the ash plume heights observed by radar. The a posteriori source term for Eyjafjallajökull  
40 consisted of gave an estimate of 0.29 Tg (with total column plume height retrievals) or 0.33 Tg (with total column retrievals  
41 only) erupted  $\text{SO}_2\text{SO}_2$  of which 95% was injected below 11 (12) km.

## 42 1 Introduction

43 Sulphur dioxide ( $\text{SO}_2\text{SO}_2$ ) is one of the major gas-phase species released in volcanic eruptions. Large  $\text{SO}_2\text{SO}_2$  releases  
44 pose a hazard to aviation, decrease air quality, and as precursors to sulphate aerosols, have a potential impact on the Earth's  
45 radiative balance (Bernard and Rose, 1990; Robock, 2000; Schmidt et al., 2015). Volcanic  $\text{SO}_2\text{SO}_2$  plumes can be detected  
46 by satellite instruments measuring in either UV or IR wavelengths - however, reliably forecasting the atmospheric transport  
47 of volcanic plumes is hindered by the lack of in-situ measurements to characterise the emission fluxes of volcanic species  
48 (Carn et al., 2009; Stohl et al., 2011; Zehner, 2012).

49 While methods based purely on satellite retrievals (Theys et al., 2013 and references therein) exist for inferring the total  
50  $\text{SO}_2\text{SO}_2$  flux for a given eruption, a successful prediction of volcanic tracers generally requires information also on the  
51 vertical profile of emissions. An important technique for assessing both vertical and temporal distribution of the emission  
52 fluxes is provided by inverse dispersion modelling, first demonstrated for volcanic emissions by Eckhardt et al. (2008).

53 The previous studies on inverse modelling of volcanic emissions has have been based on using total column retrievals of  
54  $\text{SO}_2\text{SO}_2$  or volcanic ash together with a Lagrangian (Kristiansen et al., 2010; Stohl et al., 2011) or Eulerian (Boichu et al.,  
55 2013; Boichu and Clarisse, 2014) dispersion models. In addition, Flemming and Inness (2013) devised a trajectory based  
56 scheme to evaluate the vertical emission profile, which was used together with assimilation of  $\text{SO}_2\text{SO}_2$  retrievals with the  
57 IFS (Integrated Forecast System) weather prediction system. The previous studies have demonstrated that the vertical  
58 distribution of emissions can be inferred from total column retrievals in presence of sufficient vertical wind shear. However,  
59 in the case of the Eyjafjallajökull eruption in 2010, both Boichu et al. (2013) and Flemming and Inness (2013) pointed out a  
60 lack of wind shear and a subsequent difficulty at estimating the vertical distribution of emissions.

61 Retrievals of  $\text{SO}_2\text{SO}_2$  plume height have been performed with various satellite instruments (Carboni et al., 2012; Rix et  
62 al., 2012). Nevertheless, only a few studies have incorporated these data into models. Wang et al. (2013) derived a three-  
63 dimensional  $\text{SO}_2\text{SO}_2$  distribution from retrievals by the Ozone Monitoring Instrument (OMI), and used the distribution to

64 initialize CTM simulations for the 2008 eruption of Kasatochi. Wilkins et al. (2015) used 1D-Var ash retrievals for  
65 initialising dispersion simulations. However, neither of the studies used plume height retrievals in inverse modelling of  
66 volcanic emissions.

67 The first objective of the present paper is to assess the usefulness of assimilating  $\text{SO}_2/\text{SO}_2$  plume height retrievals from the  
68 Infrared Atmospheric Sounding Interferometer (IASI) instrument in a source term inversion. Throughout this paper, the term  
69 plume height will refer to the vertical centre of mass, which is consistent with the IASI retrievals of this study. Following  
70 this definition of plume height, we introduce In Section 3.2 ~~we develop~~ an observation operator for the vertical centre of  
71 mass.

72 Since the observation operator only depends on the centre of mass and column loading, the vertical profile is only partly  
73 constrained. However, in contrast to the previous studies, this approach makes no further assumptions about the shape or  
74 thickness of the  $\text{SO}_2/\text{SO}_2$  layer. This could be advantageous, since volcanic ash or  $\text{SO}_2/\text{SO}_2$  layers vary considerably in depth  
75 (Dacre et al., 2014) and can be emitted in multiple, overlapping layers (Kristiansen et al., 2010). Although the variability of  
76 the vertical profiles may introduce uncertainty into the retrieval of the plume height, by assimilating only the centre of mass,  
77 we avoid forcing the model into a prescribed vertical profile whose uncertainty may be difficult to quantify. In  
78 addition contrast, our approach makes full use of the retrieval error estimates provided with the IASI data for both column  
79 mass and plume height, including the estimated correlation between plume height and mass errors.

80 The second objective of this paper is to explore the connection between the source term inversion and the 4D-Var data  
81 assimilation widely used in numerical weather prediction. Elbern et al. (2000) showed that the 4D-Var assimilation method  
82 (Le Dimet and Talagrand, 1986) can be easily extended into estimating emission fluxes with a chemistry transport model.  
83 Elbern et al. (2007) further evaluated the joint estimation of emission flux and airborne concentration as a strategy for  
84 improving air quality forecasts. However, in this study, the 4D-Var method is formulated to include only the emission  
85 forcing, which Under the assumption of a linear dispersion model and observations, the 4D-Var formulation results in a least  
86 squares problem similar to that solved by many existing inversion algorithms. ~~However,~~ the iterative solution employed in  
87 4D-Var favours a different regularisation approach, which is ~~discussed~~ compared in Section ~~4~~ to a more classical  
88 regularisation technique.

89 Finally, we test the variational inversion method and assimilation of plume height retrievals for estimating temporal and  
90 vertical distribution of  $\text{SO}_2/\text{SO}_2$  emission during the 2010 eruption of Eyjafjallajökull. Results of the inversion, presented in  
91 Section 5, indicate that although the vertical distribution of emissions is mostly constrained by the total column retrievals  
92 and the meteorological conditions, assimilation of plume height retrievals results in more vertically concentrated emission  
93 profile. In particular, emissions above 8-10 km between 5 and 9 May are reduced substantially, which is consistent with  
94 ~~radar-based estimates~~ the observations of the eruption column height.

## 95 2 Model setup and observational data

### 96 2.1 Dispersion model

97 The transport and removal of  $\text{SO}_2\text{SO}_2$  was evaluated using the dispersion model SILAM (System for integrated modelling  
98 of atmospheric composition; Sofiev et al., 2015, <http://silam.fmi.fi>) version 5.3. The model includes chemical removal of  
99  $\text{SO}_2\text{SO}_2$  as described by Sofiev (2000) with the OH climatology of Spivakovsky et al. (2000). The computations were driven  
100 by the ERA-Interim meteorological reanalysis (Dee et al., 2011) except for evaluating the simulated satellite retrievals  
101 described in Section 4, where operational ECMWF forecasts were used.

102 SILAM includes a variational data assimilation module, which was previously used for assimilation of air quality  
103 monitoring data of  $\text{SO}_2\text{SO}_2$  by Vira and Sofiev (2012). ~~The same 4D-Var implementation, including the adjoint codes, is~~  
104 ~~used in this study~~~~This study uses the same assimilation system~~, but instead of estimating a refinement for a regional emission  
105 inventory, we seek to reconstruct the emissions for a single volcanic eruption as a function of time and injection height.

106 The model was configured for a domain covering 50°E to 30°W and 30°N to 80°N. Horizontal resolution of 0.5°  
107 was used for the inversion, while the a posteriori simulations were run with a higher 0.25° resolution. The vertical ~~discretisation~~  
108 ~~grid~~ consists of 34 terrain-following z-levels with a 500 m resolution at the top of the domain increasing to 50 m near the  
109 surface.

### 110 2.2 ~~Observations:~~ The IASI dataset

111 IASI is an infrared Fourier transform interferometer that measures in the spectral range 645–2760  $\text{cm}^{-1}$  with spectral  
112 sampling of 0.25  $\text{cm}^{-1}$  (apodized spectral resolution of 0.5  $\text{cm}^{-1}$ ) and has global coverage every 12h. The lev1b dataset from  
113 EUMETSAT/CEDA archive is used in this study.

114 The algorithm ~~and the and the IASI  $\text{SO}_2$  dataset (column amount and altitude)dataset~~ are explained in more detail by  
115 Carboni et al. (2012). The same algorithm has been applied to other volcanic eruptions and successfully compared with other  
116 datasets (Carboni et al., 2016; Fromm et al., 2014; Koukouli et al., 2014; Schmidt et al., 2015; Spinetti et al., 2014).

117 The main points of the retrieval scheme are:

118 Retrievals are performed for the pixels that were identified by the  $\text{SO}_2\text{SO}_2$  detection scheme (Walker et al 2011, 2012).

119 All the channels between 1100-1200 and 1300-1410  $\text{cm}^{-1}$  are used in the iterative optimal estimation retrieval scheme to  
120 obtain  $\text{SO}_2\text{SO}_2$  column amount and altitude of the plume (in pressure, under the assumption that the vertical concentration of  
121  $\text{SO}_2\text{SO}_2$  follows a Gaussian distribution) together with the surface temperature. The scheme determines the column amount  
122 and ~~effective~~-altitude (mean of a Gaussian profile) of the  $\text{SO}_2\text{SO}_2$  plume with high precision (up to 0.3 DU error in  $\text{SO}_2\text{SO}_2$   
123 amount if the plume is near the tropopause), and it is well suited for plumes in ~~lower~~ troposphere.

124 The IASI  $\text{SO}_2\text{SO}_2$  retrieval is not affected by underlying cloud. If the  $\text{SO}_2\text{SO}_2$  is within or below an ash or cloud layer its  
125 signal will be masked and the retrieval will underestimate the  $\text{SO}_2\text{SO}_2$  amount. In the case of ash this is discernible a  
126 posteriori by the value of the cost function. The altitude retrieved for the Eyjafjallajökull eruption plume (using the same

127 dataset as in this paper) in the presence of underlying cloud is consistent with the CALIPSO vertical backscatter profile  
128 (Carboni et al 2016, Figs. 1,2,3).

129 A comprehensive error budget for every pixel is included in the retrieval. This is derived from an error covariance matrix  
130  $S_e$  that is based on the SO<sub>2</sub>SO<sub>2</sub>-free climatology of the differences between the IASI and forward modelled spectra.

131 Note that the error covariance,  $S_e$ , is defined to represent the effects of atmospheric variability not represented in the  
132 forward model, as well as instrument noise. This includes the effects of cloud and trace-gases which are not explicitly  
133 modelled. The matrix is constructed from differences between forward model calculations (for clear-sky) and actual IASI  
134 observations for wide range of conditions, when we are confident that negligible amounts of SO<sub>2</sub>SO<sub>2</sub> are present. It follows  
135 that a rigorous error propagation, including the incorporation of forward model and forward model parameter error, is built  
136 into the system, providing quality control and error estimates on the retrieved state. The retrieval state error covariance  
137 matrix, used for the assimilation in this work, is directly provided as output of the retrieval pixel by pixel.

### 138 2.3 Other observations

139 Section 5 presents comparisons of the a posteriori simulation and the source term with the IASI plume height and total  
140 column observations. However, additional datasets required used for evaluating vertical structure of the inversion results.  
141 Due to the scarcity of vertically resolved SO<sub>2</sub> data, the comparison is based on aerosol observations. The vertical profiles of  
142 the emitted plumes are compared with the backscatter profiles by a satellite-borne lidar, and the SO<sub>2</sub> injection height is  
143 compared to plume top time series obtained with a C-band weather radar. The potentially different emission and transport of  
144 volcanic ash and SO<sub>2</sub> introduces some ambiguity to the comparisons; however, as found in Section 5, the different data  
145 sources together with the IASI retrievals nevertheless form a fairly coherent picture. This supports the conclusion of  
146 (Thomas and Prata, (2011), who found that ash and SO<sub>2</sub> were mostly collocated with each other during the Eyjafjallajökull  
147 eruption.

148 The Cloud-Aerosol Lidar with Orthogonal Polarization (CALIOP) instrument (Winker et al., 2009) on board the  
149 CALIPSO satellite is near-nadir viewing, two-wavelength, polarisation-sensitive lidar. The comparisons in this study are  
150 shown for the 532 nm total backscatter. Hence, two main challenges are involved in using lidar data for evaluation of  
151 simulated SO<sub>2</sub> plumes. First, the comparison relies on the assumption that the SO<sub>2</sub> plume is collocated with an aerosol plume  
152 consisting either of primary particles (mainly volcanic ash) emitted in the eruption, or secondary particles (mainly sulphates)  
153 formed during the transport. Second, the volcanic plumes need to be distinguished from water or ice clouds. Although the  
154 vertical feature mask available with the CALIOP products provides a classification of aerosol and cloud types, as pointed out  
155 (Liu et al.; (2009) and (Winker et al.; (2012), thick volcanic ash plumes are frequently misclassified as ice clouds by the  
156 standard algorithm.

157 The comparisons shown in Section 5 and Appendix A consist of CALIOP overpasses intersecting the simulated  
158 Eyjafjallajökull plumes. Cases where the CALIOP track is parallel to the plume are omitted, because this makes the profiles  
159 extracted from the model very sensitive to horizontal displacement errors. Three of the CALIOP profiles have been

Formatted: Heading 2

Field Code Changed

160 collocated with the IASI retrievals under the criteria of less than 2 h time difference and less than 150 km horizontal  
161 displacement. The three collocated CALIOP tracks were previously analysed for SO<sub>2</sub> by (Carboni et al., (2016) along with  
162 two additional ones for May 14 and 16; these tracks only intersected the edge of the SO<sub>2</sub> plume and did not offer a useful  
163 comparison with the model.

164 The estimated SO<sub>2</sub> injection height is compared to the observations of plume top described by (Arason et al., (2011). The  
165 dataset includes two plume top time series, one estimated from a C-band weather radar located at the Keflavik airport 155  
166 km from the volcano, and one estimated from imagery taken with a web camera located 34 km from the volcano. The 5-  
167 minute radar data and the hourly web camera data are averaged in time to facilitate the comparison with the estimated  
168 emission. The radar data include values which indicate presence of a plume below the lowest observed height, and in order  
169 to maintain consistency with the published 6-hourly time series (Arason et al., 2011; Petersen et al., 2012a), and to avoid a  
170 high bias in the averaged values, the altitude of 2.5 km above sea level is assigned to these points.

171 Both datasets represent the highest altitude with measurable signal from the volcanic plume, and thus, the observed plume  
172 height might differ from the midpoint of the emitted layer. The radar data are consequently compared with 80th and 95th  
173 percentiles (altitudes with 80 or 95 % mass emitted below) of the emission.  
174

#### 175 2.32.4 Inversion experiments

176 The inversion algorithm is evaluated with two sets of experiments based on the eruption of Eyjafjallajökull in 2010. The  
177 eruption has been described in detail by Gudmundsson et al. (2012). The experiments covered the time between 1 and 21  
178 May, 2010, which as shown by Flemming and Inness (2013) included the most significant ~~SO<sub>2</sub>~~SO<sub>2</sub> releases.

179 The observation operator and the variational inversion technique were first evaluated in experiments with synthetic data  
180 (Section 4), where the simulated observations mimicking the IASI retrievals are extracted from a model simulation. The  
181 simulations are repeated for several assumed artificial source terms. The synthetic experiments evaluate the impact of  
182 assimilating plume height retrievals in addition to total columns, and additionally compare two options for regularising the  
183 inverse problem.

184 The IASI data were subsequently assimilated to invert for the SO<sub>2</sub> emissions ~~for~~in the Eyjafjallajökull ~~(2010)~~ eruption.  
185 The inversion was performed both with and without assimilation of the plume height retrievals keeping the setups otherwise  
186 identical.

187 3—In all inversion experiments, the emission flux density (kg m<sup>-1</sup> s<sup>-1</sup>) was estimated for each model level in steps of 12  
188 hours. The model setup used in the synthetic experiments was otherwise identical to that used with the IASI data, but a lower  
189 vertical resolution of 1 km was used to reduce the computational cost.  
190

Formatted: Normal

191

Formatted: Heading 1

192 **4.3 Assimilation and inversion methods**

193 The forward problem for volcanic tracer transport is defined by the advection-diffusion equation: given the emission  
194 forcing  $f$ , solve

195 (1) 
$$\frac{\partial c}{\partial t} + \nabla \cdot (c\mathbf{v}) - \nabla \cdot (K\nabla c) = f(x,t) - s(c,x,t),$$

196 where  $c$  is the tracer concentration,  $\mathbf{v}$  is the wind vector,  $K$  is the turbulent diffusivity tensor, and  $s(c,x,t)$  denotes the  
197 chemical and other sinks, which in this study include the wet and dry deposition of SO<sub>2</sub> and its chemical conversion to SO<sub>4</sub>.

Formatted: Subscript

198 **4.3.1 Variational source term inversion**

199 The inverse problem discussed in this paper is to determine the forcing  $f$ , given a set of observations depending on  $c$ .  
200 We assume that Eq. (1) has been discretised, and following the common notation in data assimilation literature, we denote  
201 the tracer concentrations, collectively for all time steps, with the state vector  $\mathbf{x}$ . The state vector is related to the unknown  
202 parameter vector  $\mathbf{f}$  by the model operator  $\mathcal{M}$ , and to the observations  $\mathbf{y}$  by the observation operator  $\mathcal{H}$  as  $\mathbf{y} = \mathcal{H}(\mathbf{x}) + \boldsymbol{\epsilon}$ .

Field Code Changed

203 where  $\mathbf{x}$  denotes the true state. The random vector  $\boldsymbol{\epsilon}$  includes the effect of observation errors as well as the possible  
204 representativeness or model errors associated with  $\mathcal{H}$ .

Field Code Changed

205 ~~Finally, the vector  $\mathbf{y}$  of observations is given by the possibly non-linear observation operator  $\mathcal{H}$  as  $\mathbf{y} = \mathcal{H}(\mathbf{x}) + \boldsymbol{\epsilon}$ , where~~  
206  ~~$\boldsymbol{\epsilon}$  denotes the observation error.~~

207 If the ~~observation~~ errors follow a multivariate normal distribution with covariance matrix  $\mathbf{R}$ , then a solution to the  
208 inverse dispersion problem can be sought by maximising the likelihood function, which is equivalent to minimising the cost  
209 function

210 (2) 
$$J(\mathbf{f}) = \frac{1}{2}(\mathbf{y} - \mathcal{H}(\mathbf{x}))^T \mathbf{R}^{-1}(\mathbf{y} - \mathcal{H}(\mathbf{x})),$$

211 where  $\mathbf{x} = \mathcal{M}(\mathbf{f})$ . ~~Model errors are not explicitly included in the cost function.~~

Formatted: Indent: First line: 0,4 cm

212 The cost function assumes that the airborne concentrations, which comprise the state vector  $\mathbf{x}$ , are completely determined  
213 by the emission. Therefore, contrary to chemical data assimilation studies such as Elbern et al. (2007), no term  
214 corresponding to the concentration in the beginning of assimilation is included. This is reasonable, since the inversion is  
215 performed in a single step, and the state and observation vectors in Eq. (2) cover the whole simulated period. The total SO<sub>2</sub>  
216 loading was low in the beginning of the assimilation due to the inactive phase of eruption and initial state was therefore  
217 unlikely to affect the inversion for the emission forcing.

Field Code Changed



218 Model errors are not explicitly included in the cost function, as the relation between concentrations  $\mathbf{x}$  and the emission  $\mathbf{f}$   
219 is taken as a strong constraint. Arranging the inversion into a sequence of shorter assimilation windows with a background  
220 term for the initial state would relax this constraint at the boundaries of assimilation windows. However, this would still not  
221 allow for model errors arising within the assimilation window, and problematically, the emitted mass would no longer be  
222 conserved between the assimilation windows. Consequently, we use a single assimilation window and adopt the approach of  
223 previous studies (Seibert et al., 2011; Stohl et al., 2011), where the model uncertainty is incorporated to the observation error  
224 covariance matrix  $\mathbf{R}$ . The form of  $\mathbf{R}$  is explained in more detail in Sections 3.2 and 3.3.

225 Model errors are not explicitly included in the cost function:  $\mathbf{f}$

226 If the model and observation operators are linear, represented by matrices  $\mathbf{M}$  and  $\mathbf{H}$ , then (2) becomes a linear least-  
227 squares problem. For volcanic eruptions with a known location, the emission vector  $\mathbf{f}$  is zero almost everywhere, which  
228 makes it feasible to evaluate the matrix  $\mathbf{H}\mathbf{M}$  and solve (2) algebraically. This is the basis for inversion methods of Boichu et  
229 al. (2013), Eckhardt et al. (2008) and Lu et al. (2016).

230 As an alternative to the algebraic solution, the minimisation problem (2) can be solved with gradient-based, iterative  
231 algorithms, which avoids evaluating the matrix  $\mathbf{H}\mathbf{M}$ . In this study, the cost function is minimized using the L-BFGS-B (the  
232 limited memory Broyden-Fletcher-Goldfarb-Shanno algorithm with bound constraints) algorithm of Byrd et al. (1995) which  
233 allows constraining the solution to non-negative values. Evaluating the gradient requires solving the adjoint problem for Eq.  
234 (1).

235 The iteration is continued until a stopping criterion is satisfied, e.g. until the norm of the gradient is reduced by a  
236 prescribed factor. However, in Section 4 we will discuss truncating the iteration before formal convergence in order to  
237 control the regularization.

#### 239 4.23.2 Assimilation of plume height retrievals

240 Given the tracer concentration  $c(x, y, z)$  in three dimensions, the observation operator for column integrated mass  $m_{ij}$  is  
241 given by

242 (33) 
$$m_{ij} = \sum_{k=1}^N w_k c(x_i, y_j, z_k)$$

243 where  $x_i, y_j$  and  $z_k$  are the gridpoint coordinates and  $w_k$  denotes the thickness (in meters) of the  $k$ th model level. The layer  
244 concentrations are often weighted with an averaging kernel (Eskes and Boersma, 2003) to account for the vertically varying  
245 sensitivity of the satellite retrieval. In this work, weighting is not applied because the IASI retrievals treat the plume height  
246 explicitly.

247 In the retrievals, the plume height is represented by its centre of mass-

Formatted: Finnish

Field Code Changed

Formatted: Finnish

Field Code Changed

Formatted: Finnish

248 (4) 
$$Z_{CM,ij} = \frac{1}{m_{ij}} \sum_{k=1}^N z_k w_k c_{ijk}.$$

249 It would be possible to develop an observation operator for  $Z_{CM}$ , however, the operator would be nonlinear and only defined  
 250 for nonzero columns. These problems can be overcome by replacing the centre of mass with the first moment of mass  $mZ_{CM}$ .  
 251 Then, the observations consist of pairs  $(m_{ij}, m_{ij}Z_{CM,ij})$  given by

252 (54) 
$$\begin{pmatrix} m_{ij} \\ m_{ij}Z_{CM,ij} \end{pmatrix} = \begin{pmatrix} \sum_{k=1}^N w_k c_{ijk} \\ \sum_{k=1}^N z_k w_k c_{ijk} \end{pmatrix},$$

253 where  $z_k$  is the height of the  $k$ th model level and  $i$  and  $j$  refer to the horizontal coordinates. Transforming the observations of  
 254  $Z_{CM}$  into  $mZ_{CM}$  changes the magnitudes of observation errors, and introduces a correlation between the observation  
 255 components  $m$  and  $mZ_{CM}$ . However, this effect can be evaluated and included into the observation operator.

256 ~~The mean and standard deviation of  $m$  and  $Z_{CM}$  are denoted as  $\mu_m$ ,  $\sigma_m$  and  $\mu_z$ ,  $\sigma_z$  respectively. Denote the means~~  
 257 ~~and standard deviations of  $m$  and  $Z_{CM}$  with  $\mu_m$ ,  $\mu_z$  and  $\sigma_m$  and  $\sigma_z$ .~~ Assuming that the errors of  $m$  and  $Z_{CM}$  are normally  
 258 distributed, it can be shown that the variance of first moment equals

259 (6) 
$$\begin{aligned} \text{Var}[mZ_{CM}] &= \mu_m^2 \sigma_z^2 + \mu_z^2 \sigma_m^2 + \sigma_m^2 \sigma_z^2 \\ &+ 2\mu_m \mu_z \text{Cov}[m, Z_{CM}] \\ &+ \text{Cov}[m, Z_{CM}]^2. \end{aligned}$$

260 (5) 
$$\text{Cov}[m, mZ_{CM}] = \sigma_m^2 \mu_z + \mu_m \text{Cov}[m, Z_{CM}].$$
  
 261 Under similar assumptions, the covariance of  $m$  and  $mZ_{CM}$  becomes

262 (7) 
$$\text{Cov}[m, mZ_{CM}] = \sigma_m^2 \mu_z + \mu_m \text{Cov}[m, Z_{CM}].$$

263 (6) 
$$\text{E}[mZ_{CM}] = \mu_m \mu_z + \text{Cov}[m, Z_{CM}]$$
  
 264 Finally, the expectation of  $mZ_{CM}$  is shifted due to the correlation between retrievals of  $m$  and  $Z_{CM}$ :

265 (8) 
$$\text{E}[mZ_{CM}] = \mu_m \mu_z + \text{Cov}[m, Z_{CM}]$$

266 (7) 
$$\text{E}[mZ_{CM}] = \mu_m \mu_z + \text{Cov}[m, Z_{CM}]$$
  
 267 The retrieval errors of different pixels are assumed to be uncorrelated. The observation error covariance matrix  $\mathbf{R}$  is  
 268 therefore block-diagonal, and its entries can be evaluated using Eqs. (6) and (7) from the retrieval error estimates  $\sigma_m$ ,  $\sigma_z$   
 269 and  $\text{Cov}[m, Z_{CM}]$ , which are all included in dataset used in this study, the known covariances of  $m$  and  $Z_{CM}$  using Eqs. (5)  
 270 and (6). However, even if the standard deviations  $m$  and  $Z_{CM}$  are known accurately, the means  $\mu_m$  and  $\mu_z$  need to be

Formatted: Indent: First line: 0 cm

Field Code Changed

Field Code Changed

Field Code Changed

Field Code Changed

Formatted: MTDisplayEquation

Field Code Changed

Formatted: Indent: First line: 0,4 cm

Formatted: MTDisplayEquation

Field Code Changed

Formatted: MTDisplayEquation

Field Code Changed

Formatted: Indent: First line: 0 cm

Field Code Changed

substituted with the observed values of  $m$  and  $Z_{CM}$ .  ~~$\mathbf{R}$~~ The impact of this approximation is evaluated numerically in Section 4.

Assimilation schemes commonly assume uncorrelated and unbiased observation errors. A non-diagonal  $\mathbf{R}$  can be introduced with a transformation of variables: define

$$\mathbf{L}^T \mathbf{L} = \mathbf{R}^{-1}$$

$$\tilde{\mathbf{y}} = \mathbf{L}(\mathbf{y} - \mathbf{b})$$

$$\tilde{\mathbf{H}} = \mathbf{L}\mathbf{H}$$

where  $\mathbf{L}^T \mathbf{L}$  is the Cholesky factorisation of the inverse observation error covariance matrix  $\mathbf{R}^{-1}$  and  $\mathbf{b} = (0, \text{Cov}[m, Z_{CM}])$  corrects for the bias according to Eq. ~~(8)~~(7). Then, substituting the transformations of Eq. ~~(9)~~(8) into the cost function (2) shows that assimilation of  $\mathbf{y}$  with the original  $\mathbf{R}$  is equivalent to assimilation of  $\tilde{\mathbf{y}}$  using the transformed observation operator  $\tilde{\mathbf{H}}$  with unit matrix in place of  $\mathbf{R}$ .

The above formulas can be implemented as a preprocessing step for the observations. In summary, the procedure is then as follows:

1. For each available IASI pixel  $i$ , evaluate the tuple  $\mathbf{y}_i - \mathbf{b}_i = (m_i, m_i Z_{CM,i} - \text{Cov}[m_i, Z_{CM,i}])$  and the corresponding 2x2 covariance matrix  $\mathbf{R}_i$ .
2. Factorise  $\mathbf{R}_i^{-1} = \mathbf{L}_i^T \mathbf{L}_i$  and transform the observations according to Eq. ~~(9)~~(8).
3. Store the transformed observations  $\tilde{\mathbf{y}}_i$  with their pixel-specific vertical weighting functions given by rows of the matrix  $\tilde{\mathbf{H}} = \mathbf{L}_i \mathbf{H}$ .

After the transformation, the observations are handled identically to regular column observations with a vertical weighting function.

### 4.3.3.3 Observation errors

The IASI retrievals used in this study include pixel-specific error estimates for total column and plume height retrievals. The estimates are derived statistically (Carboni et al., 2012) from differences between the transmission spectra computed by a forward model and those observed by IASI. Together with estimates for the correlation between plume height and total column retrieval errors, this provides the necessary input for equations ~~(6) and (7)~~(5) and ~~(6)~~(6).

The retrieval error estimates are only provided for pixels with positive  $\text{SO}_2\text{SO}_2$  detection. For the non- $\text{SO}_2\text{SO}_2$  pixels, which are assimilated as zero values, a different estimate is used, based on the detection limits estimated by Walker et al. (2012). The detection limit was translated into a standard deviation of a Gaussian random variable assuming, conservatively, a probability of 0.95 for a correct detection.

Formatted: MTDisplayEquation

Field Code Changed

Field Code Changed

Field Code Changed

Field Code Changed

299 However, performing the inversions with  $\mathbf{R}$  defined only by retrieval errors resulted in poor a posteriori agreement with  
 300 the IASI data, which suggested that the retrieval errors are not sufficient to describe the discrepancy between the simulated  
 301 and observed values. As ~~will be found shown in with~~ the synthetic experiments, the impact of model uncertainty is  
 302 significant compared to the retrieval errors, and it needs to be taken into account. The problem of model errors affecting the  
 303 inversion is discussed by Boichu et al. (2013), who found the impact to depend strongly on treatment of zero-value  
 304 observations, and consequently chose to keep only every tenth zero-valued observation.

305 In this study, the model errors are included by modifying the observation error covariance matrix, which is set to  
 306  $\mathbf{R} = \mathbf{R}_{obs} + \mathbf{R}_{model}$ , where  $\mathbf{R}_{model}$  is constant, diagonal and determined experimentally. The model error standard deviation for  
 307 total column observations is set to 2 DU for both the experiments using synthetic data (Section 4) and for the inversion for  
 308 Eyjafjallajökull (Section 5), while the model error for the plume height retrievals was set to 2 km for the synthetic  
 309 experiments and 1 km for the Eyjafjallajökull inversion. Reducing the plume height standard deviation to 1 km in the  
 310 synthetic experiments resulted in large negative bias in the total emission, while increasing the standard deviation to 2 km  
 311 did not significantly change the total emission in the inversion for Eyjafjallajökull.

312 ~~and corresponds to experimentally determined constant standard deviations of 2 DU for total column and 1 km for the~~  
 313 ~~plume height.~~

314 The model errors for plume height and total column are assumed uncorrelated and independent of the observation errors.  
 315 However, their effect is propagated to the covariance matrix for first moment according to Eq. (6)-(5). The actual model  
 316 errors evolve dynamically and are likely to be variable and correlated in space and between the plume height and total  
 317 column components; however, ~~a more advanced treatment including these effects~~ appears difficult in the current inversion  
 318 approach.

#### 319 4.4.3.4 Regularization

320 The least squares problem (2) has a unique solution only if the matrix  $\mathbf{H}\mathbf{M}$  is of full (numerical) rank. Furthermore, if  
 321  $\mathbf{H}\mathbf{M}$  is close to singular, the problem remains ill-posed, which results in a noisy solution. Consequently, some form of  
 322 regularisation has been employed in all previous works based on the least-squares approach.

323 A common option is the Tikhonov regularisation (Tikhonov, 1963; Engl et al., 2000; Tikhonov, 1963), which introduces a  
 324 penalty term into the cost function (2), which in the simplest form becomes

325 (10) 
$$J(\mathbf{f}) = \frac{1}{2}(\mathbf{y} - \mathbf{H}\mathbf{x})^T \mathbf{R}^{-1}(\mathbf{y} - \mathbf{H}\mathbf{x}) + \alpha^2 \sum_{k,n} w_k |f_{k,n}|^2$$

326 (9) ~~;~~  
 327 where the summation is over levels  $k$  and timesteps  $n$ . The weights  $w_k$  in Eq. (10)(9) are set equal to the thickness of each  
 328 model layer; this makes the penalty term consistent with its continuous counterpart  $\int f(z,t)^2 dt dz$ , which in turn ensures that  
 329 the regularisation term does not depend on the vertical discretisation.

Formatted: MTDisplayEquation  
 Field Code Changed

Field Code Changed

330 The penalty term can be modified to include a non-zero a priori source term. However, this approach is not taken in the  
331 present work. Instead, we aim to choose the level of regularisation optimally, so as to avoid excessive bias in the regularised  
332 solution. The need for regularisation depends on the coverage of observations, accuracy of the forward model as well as on  
333 the meteorological conditions controlling the dispersion. Thus, the regularisation parameter  $\alpha^2$  cannot be chosen a priori.

334 In this work, a criterion known as the L-curve (Hansen, 1992) is used for determining the amount of regularisation. In the  
335 L-curve approach, the inversion is performed with various values of  $\alpha^2$ , and the residual  $\|y - Hx\|$  is plotted as a function of  
336 the solution norm  $\|f\|$ . For ill-posed inverse problems, the curve is typically L-shaped. The residual initially reduces quickly  
337 as the regularization is relaxed, however, for some value of  $\alpha^2$ , the curve flattens and reducing the regularization further  
338 only marginally improves the fit. This point, where L-curve reaches its maximum curvature, is taken to represent the optimal  
339 regularisation. In the present study, the L-curve is evaluated without the frequently used logarithmic transformation.

340 The main advantage of the L-curve method is that it does not rely on a priori estimates for the observation error. This is  
341 useful, since in practice the discrepancy between simulated observations and the data is also affected by model errors, which  
342 are poorly known. The L-curve was, in effect, used in inverse modelling of volcanic  $\text{SO}_2$  also by Boichu et al. (2013).

343 Changing the regularisation parameter requires the minimisation to be started over, which is costly in the variational  
344 inversion scheme where each iteration requires a model integration. However, as noted by Fleming (1990) and Santos  
345 (1996), the iteration itself forms a sequence of solutions with decreasing regularisation. Thus, instead of minimising the  
346 regularised cost function (10), we iterate to minimise the original cost function (2), and truncate the iteration according to  
347 the L-curve criterion. This approach, known as regularisation by truncated iteration (Kaipio and Somersalo, 2006), or  
348 iterative regularisation (Hansen, 2010), provides a computationally efficient method to regularise large-scale inverse  
349 problems. In the following section, we show experimentally that ~~the truncated iteration such an approach~~ results in similar  
350 solutions for the source term inversion as the more common Tikhonov regularisation.

Field Code Changed

#### 351 **5.4 Experiments with synthetic data**

352 Regularisation by truncated iteration has been studied in detail especially for Krylov subspace based algorithms (Calvetti  
353 et al., 2002; Fleming, 1990; Kilmer and O'Leary, 2001). The effect of truncated iteration on quasi-Newton minimisation  
354 methods, such as the L-BFGS-B algorithm used in this work, has been studied less extensively. To evaluate the truncated  
355 iteration in comparison to Tikhonov regularisation for inverse modelling of volcanic emissions, we performed an experiment  
356 with synthetic observations extracted from forward model simulations. In addition to the comparison of regularisation  
357 methods, the synthetic experiments enable us to evaluate robustness of the L-curve method and to assess the impact of  
358 assimilation of plume height retrievals, and to quantify how model errors affect the source term estimate.

359 For the sake of computational convenience, the experiments in this section are not performed using the variational method  
360 described in Section 3.1, but instead the forward sensitivity matrix **HM** is evaluated by running a separate model simulation

361 for each component of the emission vector  $\mathbf{f}$ . The sensitivity matrix is subsequently used for evaluating the cost functions  
362 (Eq. (2) for truncated iteration, Eq. (10) for Tikhonov regularisation) and the respective gradients required by the L-BFGS-B  
363 minimisation code. Evaluating the sensitivity matrix also provided an opportunity to numerically confirm the equivalence of  
364 the matrix-based and variational inversion methods.

365 The experiments with synthetic data were set up for the same time (1 to 21 May, 2010) as the inversion for  
366 Eyjafjallajökull. The synthetic observations were evaluated by running forward simulations with a set of artificial source  
367 profiles (cases A to D) shown in the leftmost column of Figure 1. The synthetic observational data (total columns and first  
368 moments as explained in Section 3.2) correspond to the locations and times covered by the IASI overpasses during the  
369 simulated period.

370 The artificial source terms A and B are defined arbitrarily, while cases C and D are realisations of a stochastic process  
371 where the total flux (kg/s) is given by a lognormal, temporally correlated random variable and the eruption height follows the  
372 relation of Mastin et al. (2009). At each time, a piecewise constant vertical profile is assumed with a transition at 75% of  
373 height. The emission rate is distributed evenly between the two sections.

374 The simulations with artificial source terms were driven by the meteorological data valid for the simulated period.  
375 ~~However, T~~two sets of meteorological input were used: the synthetic observations were generated using the operational  
376 ECMWF forecast fields, ~~and-but~~ to simulate the effect of model errors, the sensitivity matrix ~~for-used in the~~ inversions was  
377 evaluated using the ERA-Interim as the meteorological driver. ~~Although changing the meteorological driver does not cover~~  
378 ~~all sources of model error, we expect the resulting perturbation to have statistical properties similar to the real model~~  
379 ~~uncertainty.~~

380 The effect of retrieval errors was simulated by

381 ~~For the sake of computational convenience, the experiments in this section were carried out by pre-evaluating the forward~~  
382 ~~sensitivity matrix  $\mathbf{HM}$  by running a separate model simulation for each component of the emission vector  $\mathbf{f}$ . In order to~~  
383 ~~simulate the effect of model errors, the matrix  $\mathbf{HM}$  was evaluated with both the ERA-Interim and operational ECMWF~~  
384 ~~forecast fields as meteorological drivers.~~

385 ~~The sensitivity matrix for inversions was extracted from the run with ERA-Interim meteorological data. The set of~~  
386 ~~synthetic observations of the  $\text{SO}_2$  column density, on the other hand, was evaluated from the model run based on the~~  
387 ~~operational meteorological fields and used as the data for the inversion experiments. The perturbing-simulated the extracted~~  
388 ~~(simulated) observations were perturbed with additive Gaussian noise. In order to perturb the simulated plume height~~  
389 ~~retrievals, the unperturbed simulated first moments and total columns were first converted back to the centre of mass and~~  
390 ~~total column for the pixels with column density higher than 0.2 DU in the forward run. Then, both the simulated centre of~~  
391 ~~mass and the total column were perturbed and transformed back to the (perturbed) total columns and first moments. The total~~  
392 ~~columns were perturbed with standard deviation equal to 0.1 DU + 10 % of the true values; the centres of mass were~~  
393 ~~perturbed with a constant standard deviation of 1 km. A negative correlation coefficient of -0.9 was assumed between the~~  
394 ~~perturbations to the total column and centre of mass.~~

Formatted: Not Highlight

395 The error covariance matrix used in the inversion was supplemented with 2 DU and 2 km “model error” as described in  
 396 Section 3.3. For the inversions using simulated plume height retrievals, the observation error covariance matrices were  
 397 transformed according to Eqs.(6)–(8) — using the perturbed centre of mass and total column values for  $\mu_z$  and  $\mu_m$   $\overline{H_z}$ .  
 398 —with standard deviation equal to 1 DU + 30% of the true value. The observation error covariance matrix used in the  
 399 inversion was supplemented with 2 DU “model error” as described in Section 3.3.

400 The residual and solution norms, which define the L-curves, are evaluated consistently to the penalized cost function (10)  
 401 (9):

$$\begin{aligned}
 (11) \quad & \| \mathbf{H} \mathbf{x} - \mathbf{y} \| = \sqrt{(\mathbf{H} \mathbf{x} - \mathbf{y})^T \mathbf{R}^{-1} (\mathbf{H} \mathbf{x} - \mathbf{y})} \\
 & \| \mathbf{f} \| = \sqrt{\sum_{k,n} w_k | f_{k,n} |^2} \\
 (10) \quad & \| \mathbf{H} \mathbf{x} - \mathbf{y} \| = \sqrt{(\mathbf{H} \mathbf{x} - \mathbf{y})^T \mathbf{R}^{-1} (\mathbf{H} \mathbf{x} - \mathbf{y})} \\
 & \| \mathbf{f} \| = \sqrt{\sum_{k,n} w_k | f_{k,n} |^2}
 \end{aligned}$$

404 where  $\mathbf{f}$  denotes the emission,  $\mathbf{x} = \mathbf{M} \mathbf{f}$  and  $w_k$  is the thickness of the  $k$ th model layer. To evaluate the L-curve for  
 405 Tikhonov-regularisation, the parameter  $\alpha^2$  was incremented in discrete steps given by  $\alpha_i^2 = 10^i \cdot 2^{-i}$  for  $i = 0, 1, 2, \dots$ . The L-  
 406 BFGS-B minimization method with non-negativity constraint was used for both Tikhonov regularisation and the truncated  
 407 iteration; in the case of Tikhonov regularisation, the iteration was continued ~~until convergence~~ for each  $\alpha_i^2$  either until  
 408 convergence or for maximum of 50 iterations. A zero-valued solution was always used as the first guess in the iteration.  
 409 With the truncated iteration, the weights  $w_k$ , required by Eqs. (10) and (11) ~~(9) and (10)~~, are not explicitly included in the  
 410 cost function. Instead, the same effect is achieved by transforming the parameter vector as  $f'_{k,n} = w_k^{1/2} f_{k,n}$ .

411 The point where the L-curve flattens, which is taken as the final solution, was determined numerically. First, the points  
 412  $(\| \mathbf{f} \|, \| \mathbf{H} \mathbf{x} - \mathbf{y} \|)$  are sorted according to increasing  $\| \mathbf{f} \|$ . Then, the points where the residual increases are removed, and finally,  
 413 the optimal point is chosen using the “triangle” algorithm of Castellanos et al. (2002).

414 ~~Figure 1~~ Figure 4 presents the inversion results using Tikhonov regularisation with total column observations, truncated  
 415 iteration with total column observations, and truncated iteration with total column and ~~centre of mass~~ plume height  
 416 observations. Regardless of the assumed source term or inversion method, the emission timing is well captured within the 12  
 417 h resolution. The overall vertical profiles are also recovered, however, spurious features are present especially in cases B and  
 418 C.

419 For comparison, Figure 2 presents the solution corresponding to the case B in Figure 1 but evaluated without  
 420 model errors – that is, using the same sensitivity matrix  $\mathbf{H} \mathbf{M}$  for both evaluating the observations and performing the  
 421 inversion. In this case, regularisation was not needed, and the true solution was recovered almost perfectly despite the noisy

Field Code Changed

Formatted: MTDisplayEquation

Field Code Changed

Field Code Changed

Field Code Changed

Formatted: Not Highlight

Formatted: Not Highlight

422 observations. Thus, the noise present in the estimated solutions in ~~Figure 1~~ is mainly due to model error, which  
423 affects the elements of matrix  $\mathbf{M}$ . All other results presented in this section are obtained in presence of model errors.

Formatted: Not Highlight

424  
425 Numerical evaluation of the inversion results in terms of RMSE and relative bias is presented in Table 1. The scores are  
426 evaluated for both truncated iteration and Tikhonov regularisation, each with and without plume height observations.  
427 Furthermore, two numbers are given for each case: the optimal value, corresponding to the regularisation (for Tikhonov, the  
428 value of  $\alpha^2$ , for truncated iteration, the iteration number) with lowest RMSE, and the L-curve value corresponding to the  
429 choice of regularisation as determined from the L-curve explained above. Clearly, the regularisation with optimal RMSE is  
430 not necessarily optimal with respect to bias.

431 For all cases, the optimally truncated iteration had lower RMSE than the optimally tuned Tikhonov regularisation.  
432 However, this advantage was not always realised when the truncation was determined from the L-curves, which are shown in  
433 Figs. 3 and 4. For the Tikhonov regularisation, the L-curve solution was generally closer to the optimal. The difference is  
434 caused by differing features of the L-curves for the two regularisation methods: for the Tikhonov regularisation, the L-curve  
435 forms a convex graph varying smoothly with  $\alpha^2$ , while the curves formed by the L-BFGS-B iterates are neither smooth nor  
436 even monotonous. Although points where the residual increases are omitted from the search, points with a locally large  
437 curvature remain in the curve, and such points are responsible for the under-regularised L-curve solutions in cases A and D  
438 when only total column was assimilated.

439 ~~In 34 cases out of 40, the RMSE of the solution determined from the L-curve was within 20% from the optimally~~  
440 ~~regularised solution. Of the remaining six cases, two were over-regularised and four were under-regularised.~~

441 In Figs. 3 and 4, the root mean squared error (RMSE) of the solution is shown next to each L-curve as a function of the  
442 regularisation parameter. As expected, the RMSE initially drops as the regularisation is relaxed, reaches a minimum, and  
443 eventually increases as the solution becomes contaminated by noise. This behaviour was especially clear when only total  
444 column observations were assimilated. When also centres of mass were assimilated, the minima in RMSE become weaker,  
445 and the RMSE with maximum number of iterations was only slightly higher than optimal. Thus, assimilating the centres of  
446 mass had the unintended but potentially useful side effect of making the inversion less sensitive to under-regularisation.

447  
448 Since the regularised cost function (10) favours solutions with a small squared norm, the inversion is expected to  
449 underestimate the true emission. If only total column observations are used, the underestimation remains small, being 5 –  
450 10% for the L-curve solutions with truncated iteration, and up to 15 % for the corresponding Tikhonov regularised solutions.  
451 However, when the plume height observations were included, the negative biases increased to 15-25% even when using  
452 truncated iteration.

453 Magnitude of the negative bias turned out to be sensitive to the assumed model uncertainty as described by the covariance  
454 matrix  $\mathbf{R}_{model}$ . Reducing the standard deviation for plume height errors to 1 km resulted in negative biases between 25 and



35%. As a further sensitivity test, we evaluated the effect of approximating the true values for total column and plume height with the respective observed values when transforming the observation error covariance matrix, as explained in Section 3.2. Using, unrealistically, the true values in the inversion, the relative biases were reduced to 16-21%. The RMSE was reduced by up to ~15%. It can be noted that none of the tested setups describe an observation error covariance matrix that would perfectly match the perturbations applied the simulated observations, since the model errors, simulated by using a different meteorological driver, are not well described by additive, white noise. Taking the cross-correlations and spatial variation of model errors into account might lead into different optimal  $\mathbf{R}_{\text{model}}$ .

The total emitted mass is underestimated by  $< 10\%$  for the solution from truncated and by up to about 15% for the Tikhonov regularised solution. The underestimation is expected due to the form of cost function (9). However, the inversion results show that the negative bias is not necessarily large unless the problem is regularised too strongly.

For comparison, Figure 2 presents the solution corresponding to the case B in Figure 1 but evaluated without model errors – that is, using the same sensitivity matrix  $\mathbf{H}\mathbf{M}$  for both evaluating the observations and performing the inversion. In this case, regularisation was not needed, and the true solution was recovered almost perfectly despite the noisy observations. Thus, the noise present in the estimated solutions in Figure 1 is mainly due to model error, which affects the elements of matrix  $\mathbf{M}$ .

The L-curves corresponding to each case in Figure 1 are shown in Figs. 3 and 4. The root mean squared error (RMSE) of the solution is shown next to each L-curve as a function of the regularisation parameter. When measured by the solution RMSE, an optimal regularisation indeed existed in each case. In case A, where the solution varies smoothly in time and space, the solution error is only moderately sensitive to the regularisation. The L-curve formed by the L-BFGS-B iterates is shallow in this case, which caused the algorithm to choose an unnecessarily high number of iterations. However, the negative effect on the solution quality was small. For the Tikhonov regularisation, the regularisation parameter was determined almost optimally.

The choice of regularisation was more critical in the remaining cases. In cases B and C, the L-curve has a clear plateau after initial decrease, and the chosen corner point is close to optimal for the both regularisation methods. In case D, the truncated iteration leads to a somewhat under-regularised solution similar to case A.

Outcome of the four experiments indicates that the need for regularisation varies strongly depending on the true source, whose characteristics also affect how accurately the algorithm determines the optimal regularisation. We used the stochastic source terms to evaluate this more quantitatively. Figure 5 presents the RMSE as a function of the iteration number for 40 realisations of the stochastic source term used in cases C and D. The optimal iteration numbers chosen from each L-curve are marked with stars.

Field Code Changed

Field Code Changed

Field Code Changed

Formatted: Highlight

Formatted: Highlight

Formatted: Highlight


487 The RMS errors shown in Figure 5 are normalised by the minimum error for each inversion, which shows that in most  
488 cases, the inversion was only moderately sensitive to the exact point of truncation. In 34 cases out of 40, the RMSE of the  
489 solution determined from the L-curve was within 20% from the optimally regularised solution. Of the remaining six cases,  
490 two were over-regularised and four were under-regularised.

491 While the experiments in this section were performed by pre-evaluating the matrix  $\mathbf{H}\mathbf{M}$ , in 4D-Var, the multiplications  
492 by  $\mathbf{H}\mathbf{M}$  and its transpose are replaced by forward and adjoint model evaluations. Although the approaches are formally  
493 equivalent, this change results in a slightly different sequence of iterations from which the L-curve is evaluated. To  
494 investigate this difference, we performed the inversion using the real IASI data using both approaches. The two solutions are  
495 shown in Figure 5 and Figure 6. The total released mass differs by less than 1% between the solutions, and the emission patterns  
496 are qualitatively similar. The differences for individual values, although larger, appear small compared to the inversion  
497 errors.

498 In summary, the experiment with synthetic data showed that the truncated iteration resulted in solutions similar to those  
499 obtained with the more common Tikhonov regularisation. This makes the truncated iteration, in combination with the L-  
500 curve, an attractive option for regularising the variational source term inversion. On the other hand, ~~the overall need for~~  
501 ~~regularisation depended strongly on the assumed source term.~~ No regularisation was needed in absence of model error,  
502 which indicates that the need for regularisation is likely to also depend on quality of the forward model. This emphasizes the  
503 need for a robust method to determine the appropriate regularisation according to the situation at hand.

## 504 6.5 Inversion results for Eyjafjallajökull

505 Optimising the source term following the regularisation strategy (truncated iteration) described in Section 3.4 results in  
506 satellite-derived estimates on the temporal and vertical emission profiles, as well as on the total emitted amount. The  
507 solutions presented here correspond to iterates chosen from the L-curve ~~as using the algorithm~~ described in Section 3.4. For  
508 assimilation of column mass only, the 9th iterate was chosen; with column mass and plume height assimilation, the 13th  
509 iterate was chosen. ~~Similarly to the synthetic experiments, the initial iterate was a zero solution. The L-curves are shown in~~  
510 ~~the supplementary information.~~

511   
512 Figure 6 shows the temporal and vertical distribution of the  $\text{SO}_2/\text{SO}_2$  emission obtained both with and without  
513 assimilation of plume height. The plume height time series estimated from radar and camera observations (Petersen et al.,  
514 2012b) are plotted on top of the emission distributions. ~~Both the camera and radar observations represent the top of the~~  
515 ~~visible plume, and e~~Even if the visible plume does not necessarily coincide with the  $\text{SO}_2/\text{SO}_2$  plume, the plume height  
516 observations provide an indication of the eruption activity.

517 ~~Figure 7~~ shows the vertical profile of emissions integrated over the whole period. The bulk of emissions are between 2  
518 ~~and 8 kilometres~~ km even if only column density is assimilated. Assimilating the plume height retrievals further decreases the

Formatted: Highlight

Formatted: Highlight

Formatted: Not Highlight

Formatted: Highlight

519 fraction of emissions above 8 km. When the plume height is assimilated, about 85% of total emission is estimated below 8  
520 km and about 95% below 11 km. Without assimilation of plume heights, the 95% level raises to 12 km.

521 The total released mass of SO<sub>2</sub> is 0.33 Tg when plume height is not assimilated and 0.29 Tg when plume height is  
522 assimilated. Figure 9 depicts the emission flux as a function of time and shows that while the largest difference in emission  
523 rate is during the peaks of 6th May, the assimilation of plume heights tends to decrease the emission rate throughout the  
524 eruption.

525  
526 The strongest emission occurred during 6th May. However, the vertical distribution of the peak depends on whether the  
527 plume height is assimilated. While the maximum occurs at 5-6 km, if plume height is not assimilated, secondary maxima  
528 appear at 11 km, reaching 13 km on 9th May. If plume height retrievals are assimilated, the emission above about 8 km is  
529 strongly suppressed. Similarly, on 18th May, the isolated emissions at 10 and 15 km are ~~essentially largely~~ removed when  
530 the plume height is assimilated.

531 A more quantitative view on the effect of assimilating the plume height retrievals is given by Figure 8, which compares  
532 the estimated centre of mass of the SO<sub>2</sub> emission with the retrieved plume heights. The plume heights are shown as averages  
533 within both 50 and 500 km radius from the volcano. The averages over wider area have better temporal coverage and they  
534 are likely to be less affected by unresolved temporal or spatial variations in the plume height. The retrievals with estimated  
535 error larger than 5 km are excluded from the averaging (although used in assimilation).

536 In addition, Figure 8 includes radar and camera observations of the plume top which are compared with the 80th and 95th  
537 percentiles of the emission. The 95th percentile, although formally more representative of the top of emissions, shows very  
538 large fluctuations compared to both observations and the 80th percentile, which suggests that the highest percentiles might  
539 not be a robust way to characterise the plume top in the inversion results.

540 Over the whole period, the inversion results show a larger variability of injection height in comparison to both IASI and  
541 the radar or camera time series. Between May 4 and 5 and later May 10 and 17, the average IASI retrievals and the emission  
542 centre of mass agree mostly within 1-2 km, as do the radar observations with the 80th percentile of emission. An exception is  
543 the evening of May 11 when the injection height appears overestimated, however, the total emission rate was low at that  
544 time. Assimilation of plume height retrievals had little impact on the injection height during these times.

545 Between May 6 and 10, the injection height is overestimated in comparison with both IASI and radar observations.  
546 Assimilating the plume height retrievals improves the comparison, but the injection height remains 2-5 km too high  
547 compared to the averaged IASI retrievals. A similar overestimation occurs on May 17 and 18. Assimilating the plume height  
548 again reduces the overestimation significantly on those days, however, both the centre of mass and the percentiles remain  
549 overestimated.

550 The total released mass of SO<sub>2</sub> is 0.33 Tg when the plume height is not assimilated and 0.29 Tg when the plume height is  
551 assimilated. Figure 8d, which depicts the emission flux as a function of time, shows that while the largest difference in

552 emission rate is during the peaks of 6th May, the assimilation of plume heights tends to decrease the emission rate  
553 throughout the eruption.

554  
555  
556 Figure 8 shows the vertical profile of emissions integrated over the whole period. The bulk of emissions are between 2  
557 and 8 kilometres even if only column density is assimilated. Assimilating the plume height retrievals further decreases the  
558 fraction of emissions above 8 km. When the plume height is assimilated, about 85% of total emission is estimated below 8  
559 km and about 95% below 11 km.

560 The total released mass of SO<sub>2</sub> is 0.33 Tg when plume height is not assimilated and 0.29 Tg when plume height is  
561 assimilated. Figure 9 depicts the emission flux as a function of time and shows that while the largest difference in emission  
562 rate is during the peaks of 6th May, the assimilation of plume heights tends to decrease the emission rate throughout the  
563 eruption.

564 The inversion results of Figure 7 can be compared with those in Figure 10, which are obtained by assimilating both total  
565 column and plume height but neglecting all off-diagonal observation error covariance matrix elements. The distribution of  
566 emissions differs strongly from both cases in Figure 7, and the vertical distribution remains as spread as with assimilation of  
567 total column only. The treatment of observation errors as described in Section 3.2 is therefore a necessary step for successful  
568 assimilation of the plume height retrievals.

569 The SO<sub>2</sub>SO<sub>2</sub> column densities simulated a posteriori are shown for 5-7/10 May in Figure 9 Figs. 11 and 12, along with the  
570 corresponding IASI retrievals. The overall patterns are well reproduced, although the column density is underestimated for  
571 some parts of the plume, especially on 7th-6th and 8th-7th of May. Due to the smaller total emission, the column densities  
572 are slightly lower when plume height is assimilated, however, the difference is small. Comparisons of the total columns for  
573 all 21 days are presented in the supplementary material.

574 Figure 10 shows the simulated plume height (evaluated as centre of mass) for 7-9 May, which corresponds to the period  
575 of overestimated injection height shown in Figure 8. Compared to IASI, the inversion using only total columns tends to  
576 overestimate the plume height for all three days. As expected from Figure 8, when the plume height retrievals are  
577 assimilated, the overestimation is reduced, but not entirely removed.

578 A more detailed evaluation of the vertical profiles is enabled by comparison with the CALIOP lidar backscatter data. It  
579 should be noted that the most prominent features in the CALIOP data are regular clouds; in particular, this includes the near-  
580 constant layers located at 1-2 km altitude.

581 In Figure 11, the simulated SO<sub>2</sub> concentration is plotted as contours together with the CALIOP attenuated backscatter data  
582 collected on May 6 and 8, 2010. On both days, the track segment intersects the SO<sub>2</sub> plume near its source. On May 6, this  
583 part of the volcanic plume is obscured by a cloud, but a distinctive aerosol layer is visible south of 60° N. This layer is  
584 reproduced by the model, however, the observed vertical extent is much thinner than modelled, indicating that the vertical  
585 variation of the transport was not sufficient to resolve the emission vertically. The plume height for the thickest part of the

Field Code Changed

Field Code Changed

Field Code Changed

Formatted: Not Highlight

Field Code Changed

586 plume is nevertheless reproduced within ~2 km, and hence, assimilating the plume height retrievals had only little impact on  
587 the simulated plume.

588 On May 8, the highest simulated concentrations coincide with a strong backscatter signal at 3-4 km altitude close to the  
589 emission (near 62° N). The altitude is consistent with the averaged IASI plume height retrievals shown in Figure 8, whereas  
590 the simulated vertical extent between 2 and 7.5 km is again too wide. While a second layer between 8 and 12 km is present  
591 in the CALIOP data, the horizontal extent of this feature is far too wide to represent the volcanic plume. A third simulated  
592 SO<sub>2</sub> layer is present at 13 km only if plume height retrievals are not assimilated; this demonstrates the difference of injection  
593 heights seen in Figure 8.

594 The CALIOP track on May 8 also crosses an older SO<sub>2</sub> plume around 48° N, where the simulated vertical extent is  
595 compatible with the CALIOP data. However, a prominent layer extending between 50° and 55° N is present in the CALIOP  
596 data. The layer is classified partly as cloud and partly aerosol in the CALIOP vertical feature mask (not shown), but the layer  
597 does not coincide with the simulated SO<sub>2</sub> plume. However, Figures 9 and 10 indicate that the simulated plume was  
598 erroneously displaced towards west during the evening of May 7. Taking this into account, it is feasible that the observed  
599 backscatter would be caused by the volcanic plume. The 3-4 km altitude of the layer would agree with the IASI plume height  
600 retrievals (Figure 10) and support the below 5 km injection heights indicated by the IASI and radar data in Figure 8.

601 Figures 12 through 14 combine the simulated SO<sub>2</sub> profiles and the CALIOP data with collocated IASI total column and  
602 plume height retrievals. The simulated vertical distributions are mostly consistent with both the CALIOP and the IASI data.  
603 In Figure 12, the 3-4 km mean altitude of the peak reaching 20 DU according to the IASI data is reproduced by the model.  
604 The altitude of the plume extending towards south (between 48-50° N) is also reproduced given the higher retrieval  
605 uncertainty. The column densities up to 20 DU, however, are not reproduced: the highest simulated values are displaced  
606 towards west and remain below 10 DU.

607 Figures 13 and 14 show generally similar level of agreement in the vertical structures. In both figures, the northern part of  
608 the plume (55-60° N) is partly obscured by a cloud, which is reflected by the large retrieval error estimates. In both figures,  
609 assimilating only total column retrievals resulted in several isolated SO<sub>2</sub> layers between altitudes of 10-15 km. Presence of  
610 these layers is supported by neither IASI nor CALIOP data. Even if the corresponding SO<sub>2</sub> emissions did not coincide with  
611 ash emissions, some CALIOP signal could be expected due to the sulphate particles forming in the plume. Altogether, the  
612 comparisons in Figs. 12 through 14 and the comparison of the emission profiles (Figure 8) support the conclusion that the  
613 emissions above 8-10 km on 6-9 May were an artefact and probably related to insufficient wind shear.

614 Further comparisons with CALIOP data on 14 to 17 May are shown in Appendix A. The simulated vertical distributions  
615 generally coincide with layers observed by CALIOP; however, assimilation of plume height retrievals had little impact on  
616 the simulated plumes at those times.

617 The plume height, evaluated as centre of mass, for 6-9 May is shown in Figure 13. Compared to IASI, the simulation  
618 based only on assimilation of total columns tends to overestimate the plume height for all four days. When the plume height  
619 retrievals are assimilated, the overestimation is reduced consistently, although not entirely removed.

620 **76 Discussion**

621 ~~No a priori assumptions regarding shape the emission profile were made in this study. If only total column retrievals are~~  
622 ~~used in the inversion, the estimated source term includes isolated emissions reaching up to 15 km. With plume height~~  
623 ~~assimilation, the vertical distribution becomes more concentrated and also more consistent with the plume observed with the~~  
624 ~~radar, which suggests that the vertical distribution SO<sub>2</sub> and ash emissions was mostly similar.~~

625 ~~The centre of mass retrievals only partly constrain the vertical distribution, and hence some emission remains between 8~~  
626 ~~and 12 km, and the overestimation of plume height is reduced but not removed in the a posteriori simulations. However,~~  
627 ~~given the about 1 km uncertainty in the IASI plume height retrievals and the 1 km assumed model uncertainty (Section 3.3)~~  
628 ~~included into the observation errors, the inversion results for plume height are consistent with the assumptions of the~~  
629 ~~inversion.~~

630 ~~No a priori assumptions regarding shape the emission profile were made in this study. The comparison with the~~  
631 ~~IASI retrievals, CALIOP data and weather radar observations of the plume shows that the resulting vertical distributions~~  
632 ~~were frequently in good agreement with the observations even if only total column retrievals were used in the inversion. The~~  
633 ~~most notable exception were the emissions between 6 and 10 May, when the injection height was strongly overestimated,~~  
634 ~~and although assimilating the plume height retrievals improved the agreement, the discrepancy was not fully resolved. Since~~  
635 ~~the plume height retrievals are introduced as a weak constraint, a complete match between the inversion results and the~~  
636 ~~observation data is not expected. However, some of the discrepancies remain too large to be explained by retrieval errors~~  
637 ~~even together with the assumed model 1 km uncertainty.~~

638 ~~Generally, two factors could lead to an inaccurate reconstruction of the vertical profile from the total column~~  
639 ~~observations. First, the horizontal transport patterns on different altitudes might be too similar for resolving the vertical~~  
640 ~~structure. Second, the simulated horizontal patterns might be too inaccurate due to errors or low resolution of the transport~~  
641 ~~model or its input data. Since the inversion does not allow for systematic model errors, including the plume height retrievals~~  
642 ~~in the inversion is expected to improve the vertical profile mainly in the first case. The discrepancy remaining between the~~  
643 ~~observed and modelled plume heights suggests that model errors were at least partly responsible for the overestimation of~~  
644 ~~injection heights on 6-10 May.~~

645 ~~The main effect of assimilating the plume height retrievals was the reduction of emissions above 10-12 km. Although~~  
646 ~~these emissions are not large compared to the total emission, this outcome has some qualitative significance, since without~~  
647 ~~assimilation of plume heights, some emissions would be assigned above the tropopause. In addition to the data presented in~~  
648 ~~the previous section, pPrevious studies based on Lidar-lidar observations data (Ansmann et al., 2010) or, aircraft~~  
649 ~~measurements (Schumann et al., 2011) or inverse modelling (Stohl et al., 2011) do not suggest significant injection above the~~  
650 ~~10 km altitude. However, these studies were mainly focused on volcanic ash instead of SO<sub>2</sub>SO<sub>2</sub>, and as shown by Thomas~~  
651 ~~and Prata (2011), ash and SO<sub>2</sub> were not always transported together. On the other hand, In contrast, the SO<sub>2</sub>SO<sub>2</sub> plume~~  
652 ~~height estimates derived from the GOME-2 satellite instrument by Rix et al. (2012) do indicate heights above 10 km and up~~  
~~to 13 km on 5th of May. However, Neither our data nor inverse modelling reproduces this result, as the plume heights~~

Formatted: Highlight

Formatted: Highlight

Formatted: Highlight

Formatted: Not Highlight

653 retrieved from IASI data are below 6 km for that day, which agrees with the modelled plume heights (not shown) even when  
654 only total column retrievals are included in the inversion.

655 Among the previous emissions estimates for Eyjafjallajökull, Flemming and Inness (2013) estimated a 0.25 Tg total  
656  $\text{SO}_2/\text{SO}_2$  release using GOME-2 satellite retrievals, and 0.14 Tg using the OMI retrievals. Our estimates of 0.29-0.33 Tg are  
657 higher, especially compared OMI, but this is consistent with the higher total  $\text{SO}_2/\text{SO}_2$  burden estimated (Carboni et al., 2012)  
658 from the IASI data used in this study. Using the GOME-2 data, (Flemming and Inness, (2013) furthermore estimated  $\text{SO}_2$   
659 injection heights (defined as centres of 2-3 km thick layers) to mostly between 4 and 6 km above sea level with a peak  
660 reaching 10 km on May 19th. This agrees reasonably well with our mean profile (Figure 7), although contrary to our results  
661 without plume height assimilation. Flemming and Inness (2013) did not obtain the injection heights above 6 km on May 6th  
662 and 7th.

663 (Boichu et al., (2013) used the IASI retrievals of (Clarisse et al., (2012) to invert for temporally resolved  $\text{SO}_2$  emissions of  
664 Eyjafjallajökull between May 1th and 12th, 2010, and estimated a total emission of about 0.17 Tg. Our inversion yielded for  
665 the same time 0.21 (total column and plume height retrievals) or 0.23 (total column only) Tg of  $\text{SO}_2$ . The larger total  
666 emission in our study might be due to assumptions regarding plume height in the IASI retrievals. The retrievals used by  
667 Boichu et al. (2013) assumed constant 7 km plume height, while the retrieved plume heights in this study were frequently  
668 lower especially near the volcano, and this would result in a higher retrieved values for the total column. For the emission,  
669 Boichu et al. (2013) assumed a constant injection height of 6 km, which turns out to coincide with the maximum of the mean  
670 profile (Figure 7) obtained in this study.

671 (Stohl et al., (2011) determined the temporal and vertical distribution of volcanic ash emissions for the Eyjafjallajökull  
672 eruption with an inversion constrained by SEVIRI ash retrievals and an a priori source derived from plume top observations.  
673 Although the ash and  $\text{SO}_2$  emissions cannot be compared quantitatively, the mean vertical profile obtained using ECMWF  
674 meteorological data (Fig. 2 in Stohl et al. (2011) is not very different from the one in Figure 7. In both profiles, the emissions  
675 are restricted mainly below 8 km and have maxima at 6 km.

676 Including the plume height retrievals in the inversion resulted in a total emission 12% lower than with total column  
677 retrievals only. Similar differences were observed in the experiments with synthetic data discussed in Section 4, where the  
678 inversion results were biased low by 15-20% using both plume height and total column retrievals and by only 2-10% using  
679 total columns only.

680 In ideal conditions, assimilating the plume height information should not affect the simulated total columns. However,  
681 adding a vertical constraint to the inversion can never improve the agreement for total columns, and in presence of realistic  
682 model uncertainty, a negative effect can be expected. The systematic tendency towards smaller emission may be caused by  
683 the regularisation, which penalises the quadratic norm of the solution. The synthetic experiments indicated that introducing  
684 the plume height retrievals did not allow relaxing the regularisation, since the optimal level (as identified from the parameter  
685  $\alpha^2$ ) was similar with and without the plume height observations.

Field Code Changed

Field Code Changed

686 On the other hand, the synthetic experiments also indicated that the estimation error for the total emission was only  
687 moderately sensitive to the differences of the assumed source terms. The estimate for total emission was also robust with  
688 regard to the vertical resolution, as halving the vertical resolution of the reconstruction (compare Figs. 5 and 6) resulted in  
689 only minimal change in the total emission. The estimated total emission could, nevertheless, be affected by biases in the  
690 satellite retrievals, or by model errors not exposed by the change of meteorological driver.

691  $\alpha^2$

692 The experiments with synthetic data furthermore (Section 4) showed that the need for regularisation, or in Bayesian terms,  
693 the need for a priori information, strongly depends on the situation. In addition, the need for regularisation, was strongly or in  
694 Bayesian terms, the need for a priori information, was strongly affected by uncertainty of the forward model, and the  
695 efforts needed to handle zero-valued observations in this and other studies (Boichu et al., 2013; Seibert et al., 2011) support  
696 this conclusion. The errors arising from the dispersion model are likely to be correlated in space, and therefore, introducing  
697 the corresponding non-diagonal elements in the error covariance matrix  $\mathbf{R}$  could improve the inversion results.

698 ~~The model errors resulted in noisy temporal and vertical emission profiles in the synthetic experiments and probably also in  
699 the real inversions. However, the estimates for total emission were fairly robust regardless of the assumed source term or  
700 perturbations to the forward model. Also, halving the vertical resolution of the reconstruction (compare Figs. 6 and 7)  
701 resulted in only minimal change in the total emission. Nevertheless, the estimates of the total emission could be affected by  
702 biases in the satellite retrievals, or by model errors not exposed by the change of meteorological driver.~~

703 While the regularisation used in this work is equivalent to a zero-valued a priori source, a more informative a priori source  
704 could be accommodated with a change of variables. Other forms of regularisation proposed for the volcanic source term  
705 inversion include second-order temporal smoothing (Boichu et al., 2013), which also could be handled by truncated iteration  
706 as discussed by Calvetti et al. (2002).

707 The variational inversion method is computationally efficient if high temporal or vertical resolution is desired for the  
708 reconstruction. In the current configuration, the reconstructed solution had formally 1360 degrees of freedom. Each iteration  
709 consisting of one forward and one adjoint integration, the 25 iterations would require ~~model integrations equivalent to about~~  
710 ~~about 1000 simulated days days to be simulated~~. In comparison, evaluating the matrix  $\mathbf{H}\mathbf{M}$  directly would require 1360  
711 model integrations, and if the sensitivity was evaluated in windows of e.g. 72 hours, almost 4000 simulated days would be  
712 required. ~~The matrix-based approach is, however, more easily parallelised, while the parallelisation of the variational method~~  
713 ~~relies on the dispersion model. In our configuration, one iteration took about 5 minutes wall clock time on a 20-core node of~~  
714 ~~a Cray XC30 supercomputer.~~

715 A drawback of the 4D-Var inversion method is that the a posteriori error covariance matrix for the source term is difficult  
716 to evaluate. However, Monte Carlo techniques could be used to sample the a posteriori uncertainty.

Field Code Changed

Formatted: Not Highlight

Formatted: Not Highlight

Formatted: Not Highlight

Formatted: Not Highlight

Formatted: Not Highlight

Field Code Changed

Formatted: Indent: First line: 0 cm



## 87 Conclusions

We have presented an observation operator for retrievals of the vertical centre of mass of a tracer plume. The operator is based on transforming the centre of mass into first moment of mass using the retrieval of total column. The approach was tested by performing a source term inversion using both artificial data and the  $\text{SO}_2/\text{SO}_2$  retrievals from the IASI instrument during the Eyjafjallajökull eruption in May 2010. The inverse problem was solved with the 4D-Var method embedded into the SILAM dispersion model, and the truncated iteration is proposed as an efficient regularisation method for the 4D-Var inversion. Using both real and synthetic data, the 4D-Var method was shown to produce a similar solution as the more common algebraic method, but at lower computational cost.

The inversion results for Eyjafjallajökull were compared to radar based ash plume observations and CALIOP lidar profiles. The comparisons show that assimilating the plume height retrievals reduced the overestimation of injection height during individual periods of 1-3 days. However, for most of the simulated 21 days, the injection height was constrained by meteorological conditions and assimilation of the plume height retrievals had only small impact.

Assimilating the plume height retrievals reduced the vertical spread of the  $\text{SO}_2$  injection. When the plume height was is assimilated, about 85% of the 0.29 Tg total emission was below 8 km and about 95% was below 11 km. Compared to previous modelling studies (Boichu et al., 2013; Flemming and Inness, 2013), the total emission is 15-20% larger taking into account the differences in temporal coverage of the studies.

Introducing the plume height retrievals in the inversion may have an adverse effect on the estimated total emission. In the experiment with artificial observations, the inversions with only total column data had a negative bias of 2-10% which increased to 15-20% when the plume height observations were included. In the inversion for Eyjafjallajökull, performing the inversion using only total column retrievals resulted in ~15% larger total emission, which is consistent with the experiments with simulated observations.

The injection profile obtained by assimilating the plume height retrievals is more consistent with the radar and camera based observations of the ash plume.

The inverse problem was solved with the 4D-Var method embedded into the SILAM dispersion model. Truncated iteration is proposed as an efficient regularisation method for the 4D-Var inversion. Using both real and synthetic data, the 4D-Var method was shown to produce a similar solution as the more common algebraic method, but at considerably lower computational cost.

Experiments with both synthetic and real data suggest that the inversion is sensitive to errors in the forward model, and to their assumed uncertainty. Methods more robust to model errors are a topic suitable for future research.

747 **Acknowledgements**

748 This work has been supported by the ESA projects SMASH and VAST and Nordforsk Centre of Excellence Embla. E.C  
749 and R.G.G. acknowledge funding from the NERC SHIVA (NE/J023310/1) and VANAHEIM (NE/1015592/1) projects. The  
750 work of E.C. has been partly funded by the EC-FP7 APhoRISM project. The authors thank Marje Prank for comments on the  
751 manuscript.

752 **Code availability**

753 The source code for SILAM v5.3, including the data assimilation component, is available on request from the authors  
754 ([julius.vira@fmi.fi](mailto:julius.vira@fmi.fi), [mikhail.sofiev@fmi.fi](mailto:mikhail.sofiev@fmi.fi)).

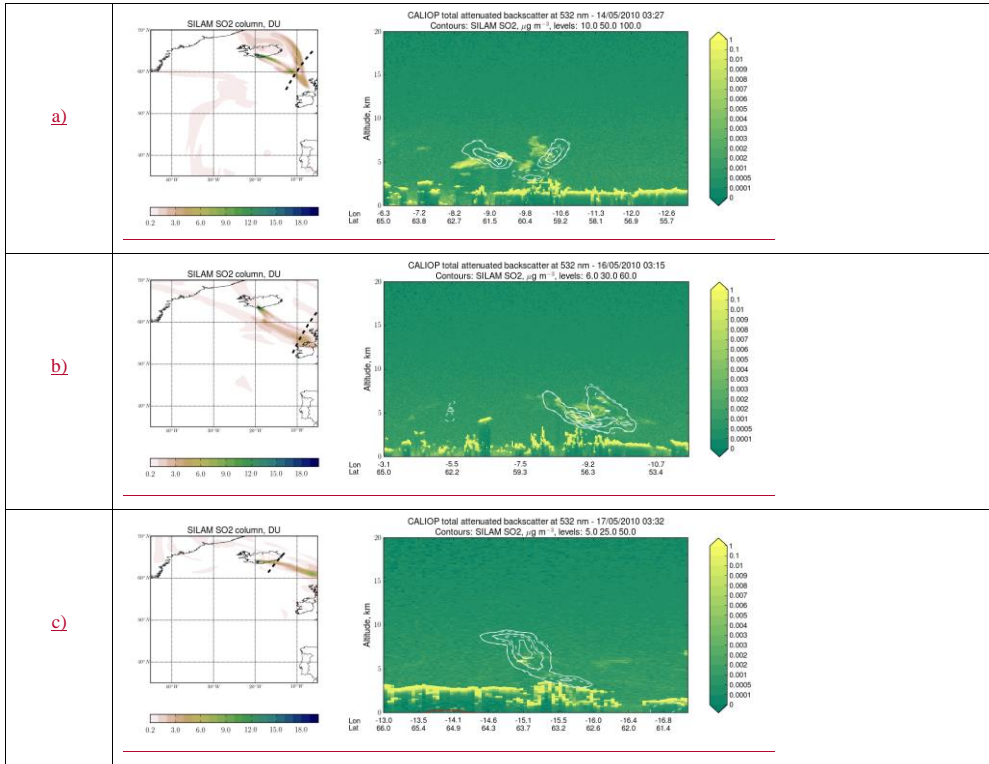
755

756

757

758

Appendix A: Additional comparisons with CALIOP data



Formatted: Left  
Formatted Table

Formatted: Left

Formatted: Left

Formatted: Normal

759

760

761

762

763

Figure A1. Comparison of simulated SO<sub>2</sub> concentration (µg m<sup>-3</sup>) compared to CALIOP total backscatter at 532 nm on 14 (panel a), 16 (b) and 17 (c) May, 2010. The inversion with only total column retrievals is shown in dashed contours. The contour levels 10, 50, and 100 in panel a, 6, 30 and 60 in panel b and 5, 25 and 50 in panel c.

764  
765  
766  
767  
768

Formatted: Normal

Formatted: Indent: First line: 0 cm

769 **Appendix B: moments of products of correlated Gaussian random variables**

770 Let  $X$  and  $Y$  be scalar random variables with means and variances  $\mu_x$ ,  $\mu_y$ ,  $\sigma_x^2$  and  $\sigma_y^2$ . Then, it follows from the  
771 definitions for variance and covariance that

772 (12+4) 
$$\text{Var}[XY] = \sigma_x^2 \sigma_y^2 + \mu_x^2 \sigma_y^2 + \mu_y^2 \sigma_x^2 - 2\mu_x \mu_y \text{Cov}[X, Y] - \text{Cov}[X, Y]^2 + \text{Cov}[X^2, Y^2]$$

773 and

774 (13+2) 
$$\text{Cov}[X, XY] = E[X^2]E[Y] + \text{Cov}[X^2, Y] - E[X]E[XY] .$$

775 To expand  $\text{Cov}[X^2, Y^2]$  and  $\text{Cov}[X^2, Y]$  we assume that  $X$  and  $Y$  are normally distributed. We first define normalized  
776 auxiliary variables

777 (14+3) 
$$\tilde{X} = \frac{X - \mu_x}{\sigma_x}, \tilde{Y} = \frac{Y - \mu_y}{\sigma_y} .$$

778 Then, by expressing  $\tilde{Y}$  as

779 (15+4) 
$$\tilde{Y} = c\tilde{X} + \sqrt{1 - c^2}\tilde{Z} ,$$

780 where  $c = \text{Cov}[\tilde{X}, \tilde{Y}]$  and  $\tilde{Z} \sim \mathcal{N}(0, 1)$  independent of  $\tilde{X}$ , it is simple to verify that

781 (16+5) 
$$\begin{aligned} \text{Cov}[\tilde{X}^2, \tilde{Y}^2] &= 2c^2 \\ \text{Cov}[\tilde{X}^2, \tilde{Y}] &= 0. \end{aligned}$$

782 For the original random variables  $X$  and  $Y$ , we find by substituting (14)+(13) into the definition, expanding the terms, and  
783 using identities (16)+(15) that

784 (17+6) 
$$\text{Cov}[X^2, Y^2] = 2\text{Cov}[X, Y]^2 + 4\mu_x \mu_y \text{Cov}[X, Y]$$

785 and

786 (18+7) 
$$\text{Cov}[X^2, Y] = 2\mu_x \text{Cov}[X, Y] .$$

787 Formulas (5) and (6) now follow by combining Eqs. (17)+(6) and (18)+(7) with (12)+(4) and (13)+(2).

Field Code Changed

Field Code Changed

790 **References**

- 791 Ansmann, A., Tesche, M., Groß, S., Freudenthaler, V., Seifert, P., Hiebsch, A., Schmidt, J., Wandinger, U., Mattis, I.,  
792 Müller, D., Wiegner, M., 2010. The 16 April 2010 major volcanic ash plume over central Europe: EARLINET lidar  
793 and AERONET photometer observations at Leipzig and Munich, Germany. *Geophys. Res. Lett.* 37, 1–5.  
794 doi:10.1029/2010GL043809
- 795 Arason, P., Petersen, G.N., Bjornsson, H., 2011. Observations of the altitude of the volcanic plume during the eruption of  
796 Eyjafjallajökull, April–May 2010. *Earth Syst. Sci. Data* 3, 9–17. doi:10.5194/essdd-4-1-2011
- 797 Bernard, A., Rose, W.I., 1990. The injection of sulfuric acid aerosols in the stratosphere by the El Chichón volcano and its  
798 related hazards to the international air traffic. *Nat. Hazards* 3, 59–67. doi:10.1007/BF00144974
- 799 Boichu, M., Clarisse, L., 2014. Improving volcanic sulfur dioxide cloud dispersal forecasts by progressive assimilation of  
800 satellite observations. *Geophys. Res. Lett.* 41, 2637–2643. doi:10.1002/2014GL059496.Abstract
- 801 Boichu, M., Menut, L., Khvorostyanov, D., Clarisse, L., Clerbaux, C., Turquety, S., Coheur, P.-F., 2013. Inverting for  
802 volcanic SO<sub>2</sub> flux at high temporal resolution using spaceborne plume imagery and chemistry-transport modelling:  
803 the 2010 Eyjafjallajökull eruption case study. *Atmos. Chem. Phys.* 13, 8569–8584. doi:10.5194/acp-13-8569-2013
- 804 Byrd, R.H., Lu, P., Nocedal, J., Zhu, C., 1995. A limited memory algorithm for bound constrained optimization. *SIAM J.*  
805 *Sci. Comput.* 16, 1190–1208.
- 806 Calvetti, D., Lewis, B., Reichel, L., 2002. GMRES, L-curves, and discrete ill-posed problems. *BIT Numer. Math.* 42, 44–65.
- 807 Carboni, E., Grainger, R., Walker, J., Dudhia, a., Siddans, R., 2012. A new scheme for sulphur dioxide retrieval from IASI  
808 measurements: application to the Eyjafjallajökull eruption of April and May 2010. *Atmos. Chem. Phys.* 12, 11417–  
809 11434. doi:10.5194/acp-12-11417-2012
- 810 Carboni, E., Grainger, R.G., Mather, T.A., Pyle, D.M., Thomas, G., Siddans, R., Smith, A., Dudhia, A., Koukouli, M.L.,  
811 Balis, D., 2016. The vertical distribution of volcanic SO<sub>2</sub> plumes measured by IASI. *Atmos. Chem. Phys.* 16,  
812 4343–4367. doi:doi:10.5194/acp-16-4343-2016
- 813 Carn, S.A., Krueger, A.J., Krotkov, N.A., Yang, K., Evans, K., 2009. Tracking volcanic sulfur dioxide clouds for aviation  
814 hazard mitigation. *Nat. Hazards* 51, 325–343. doi:10.1007/s11069-008-9228-4
- 815 Castellanos, J.L., Gómez, S., Guerra, V., 2002. The triangle method for finding the corner of the L-curve ☆. *Appl. Numer.*  
816 *Math.* 43, 359–373.
- 817 Clarisse, L., Hurtmans, D., Clerbaux, C., Hadji-Lazarou, J., Ngadi, Y., Coheur, P.-F., 2012. Retrieval of sulphur dioxide from  
818 the infrared atmospheric sounding interferometer (IASI). *Atmos. Meas. Tech.* 5, 581–594.
- 819 Dacre, H.F., Grant, A.L.M., Harvey, N.J., Thomson, D.J., Webster, H.N., Marengo, F., 2014. Volcanic ash layer depth:  
820 Processes and mechanisms. *Geophys. Res. Lett.* 42. doi:10.1002/2014GL062454
- 821 Dee, D.P., Uppala, S.M., Simmons, a. J., Berrisford, P., Poli, P., Kobayashi, S., Andrae, U., Balmaseda, M. a., Balsamo, G.,  
822 Bauer, P., Bechtold, P., Beljaars, a. C.M., van de Berg, L., Bidlot, J., Bormann, N., Delsol, C., Dragani, R., Fuentes,  
823 M., Geer, a. J., Haimberger, L., Healy, S.B., Hersbach, H., Hólm, E. V., Isaksen, L., Kållberg, P., Köhler, M.,  
824 Matricardi, M., McNally, a. P., Monge-Sanz, B.M., Morcrette, J.-J., Park, B.-K., Peubey, C., de Rosnay, P., Tavolato,  
825 C., Thépaut, J.-N., Vitart, F., 2011. The ERA-Interim reanalysis: configuration and performance of the data  
826 assimilation system. *Q. J. R. Meteorol. Soc.* 137, 553–597. doi:10.1002/qj.828
- 827 Eckhardt, S., Prata, A.J., Seibert, P., Stebel, K., Stohl, A., 2008. Estimation of the vertical profile of sulfur dioxide injection

- 828 into the atmosphere by a volcanic eruption using satellite column measurements and inverse transport modeling.  
829 Atmos. Chem. Phys. 8, 3881–3897. doi:10.5194/acpd-8-3761-2008
- 830 Elbern, H., Schmidt, H., Talagrand, O., Ebel, a., 2000. 4D-variational data assimilation with an adjoint air quality model for  
831 emission analysis. Environ. Model. Softw. 15, 539–548. doi:10.1016/S1364-8152(00)00049-9
- 832 Elbern, H., Strunk, A., Schmidt, H., Talagrand, O., 2007. Emission rate and chemical state estimation by 4-dimensional  
833 variational inversion. Atmos. Chem. Phys. 7, 3749–3769. doi:10.5194/acpd-7-1725-2007
- 834 Engl, H.W., Hanke, M., Neubauer, A., 2000. Regularization of Inverse Problems, Mathematics and Its Applications.  
835 Springer Netherlands.
- 836 Eskes, H.J., Boersma, K.F., 2003. Averaging kernels for DOAS total-column satellite retrievals. Atmos. Chem. Phys. 3,  
837 1285–1291.
- 838 Fleming, H.E., 1990. Equivalence of regularization and truncated iteration in the solution of ill-posed image reconstruction  
839 problems. Linear Algebra Appl. 130, 133–150. doi:10.1016/0024-3795(90)90210-4
- 840 Flemming, J., Inness, A., 2013. Volcanic sulfur dioxide plume forecasts based on UV-satellite retrievals for the 2011  
841 Grímsvötn and the 2010 Eyjafjallajökull eruption. J. Geophys. Res. Atmos. 118. doi:10.1002/jgrd.50753
- 842 Fromm, M., Kablick, G., Nedoluha, G., Carboni, E., Grainger, R., Campbell, J., Lewis, J., 2014. Correcting the record of  
843 volcanic stratospheric aerosol impact: Nabro and Sarychev Peak. J. Geophys. Res. Atmos. 119, 10,343-10,364.  
844 doi:10.1002/2014JD021507
- 845 Gudmundsson, M.T., Thordarson, T., Höskuldsson, A., Larsen, G., Björnsson, H., Prata, F.J., Oddsson, B., Magnússon, E.,  
846 Högnadóttir, T., Petersen, G.N., Hayward, C.L., Stevenson, J. a, Jónsdóttir, I., 2012. Ash generation and distribution  
847 from the April-May 2010 eruption of Eyjafjallajökull, Iceland. Sci. Rep. 2. doi:10.1038/srep00572
- 848 Hansen, P.C., 2010. Discrete Inverse Problems: Insight and Algorithms, Fundamentals of Algorithms. Society for Industrial  
849 and Applied Mathematics.
- 850 Hansen, P.C., 1992. Analysis of Discrete Ill-Posed Problems by Means of the L-Curve. SIAM Rev. 34, 561–580.  
851 doi:10.1137/1034115
- 852 Kaipio, J., Somersalo, E., 2006. Statistical and Computational Inverse Problems, Applied Mathematical Sciences. Springer  
853 New York.
- 854 Kilmer, M.E., O’Leary, D.P., 2001. Choosing Regularization Parameters in Iterative Methods for Ill-Posed Problems. SIAM  
855 J. Matrix Anal. Appl. 22, 1204–1221. doi:10.1137/S0895479899345960
- 856 Koukoulis, M.E., Clarisse, L., Carboni, E., van Gent, J., Spinetti, C., Balis, D., Dimopoulos, S., Grainger, R., Theys, N.,  
857 Tampellini, L., Zehner, C., 2014. Intercomparison of Metop-A ~~SO<sub>2</sub>~~SO<sub>2</sub> measurements during the 2010-2011 Icelandic  
858 eruptions. Ann. Geophys. Fast Track. doi:10.4401/ag-6613
- 859 Kristiansen, N.I., Stohl, A., Prata, A.J., Richter, A., Eckhardt, S., Seibert, P., Hoffmann, A., Ritter, C., Bitar, L., Duck, T.J.,  
860 Stebel, K., 2010. Remote sensing and inverse transport modeling of the Kasatochi eruption sulfur dioxide cloud. J.  
861 Geophys. Res. 115, 1–18. doi:10.1029/2009JD013286
- 862 Le Dimet, F.-X., Talagrand, O., 1986. Variational algorithms for analysis and assimilation of meteorological observations:  
863 theoretical aspects. Tellus A 38A, 97–110. doi:10.1111/j.1600-0870.1986.tb00459.x
- 864 Liu, Z., Vaughan, M., Winker, D., Kittaka, C., Getzewich, B., Kuehn, R., Omar, A., Powell, K., Trepte, C., Hostetler, C.,  
865 2009. The CALIPSO lidar cloud and aerosol discrimination: Version 2 algorithm and initial assessment of  
866 performance. J. Atmos. Ocean. Technol. 26, 1198–1213. doi:10.1175/2009JTECHA1229.1
- 867 Lu, S., Lin, H.X., Heemink, A.W., Fu, G., Segers, A.J., 2016. Estimation of Volcanic Ash Emissions Using Trajectory-

Formatted: Swedish (Sweden)

868 Based 4D-Var Data Assimilation. *Mon. Weather Rev.* 144, 575–589. doi:10.1175/MWR-D-15-0194.1

869 Mastin, L.G., Guffanti, M., Servranckx, R., Webley, P., Barsotti, S., Dean, K., Durant, a., Ewert, J.W., Neri, a., Rose, W.I.,  
870 2009. A multidisciplinary effort to assign realistic source parameters to models of volcanic ash-cloud transport and  
871 dispersion during eruptions. *J. Volcanol. Geotherm. Res.* 186, 10–21. doi:10.1016/j.jvolgeores.2009.01.008

872 Petersen, G.N., Bjornsson, H., Arason, P., 2012a. The impact of the atmosphere on the Eyjafjallajökull 2010 eruption plume.  
873 *J. Geophys. Res. Atmos.* 117, 1–14. doi:10.1029/2011JD016762

874 Petersen, G.N., Bjornsson, H., Arason, P., von Löwis, S., 2012b. Two weather radar time series of the altitude of the  
875 volcanic plume during the May 2011 eruption of Grímsvötn, Iceland. *Earth Syst. Sci. Data* 4, 121–127.  
876 doi:10.5194/essd-5-281-2012

877 Rix, M., Valks, P., Hao, N., Loyola, D., Schlager, H., Huntrieser, H., Flemming, J., Koehler, U., Schumann, U., Inness, A.,  
878 2012. Volcanic SO<sub>2</sub>SO<sub>2</sub>, BrO and plume height estimations using GOME-2 satellite measurements during the  
879 eruption of Eyjafjallajökull in May 2010. *J. Geophys. Res. Atmos.* 117. doi:10.1029/2011JD016718

880 Robock, A., 2000. Volcanic eruptions and climate. *Rev. Geophys.* 38, 191–219.

881 Santos, R.J., 1996. Equivalence of regularization and truncated iteration for general ill-posed problems. *Linear Algebra*  
882 *Appl.* 236, 25–33.

883 Schmidt, A., Leadbetter, S., Theys, N., Carboni, E., Witham, C.S., Stevenson, J.A., Birch, C.E., Thordarson, T., Turnock, S.,  
884 Barsotti, S., Delaney, L., Feng, W., Grainger, R.G., Hort, M.C., Höskuldsson, Á., 2015. Satellite detection, long-range  
885 transport and air quality impacts of sulfur dioxide from the 2014-2015 flood lava eruption at Bárðarbunga (Iceland). *J.*  
886 *Geophys. Res. Atmos.* 120, 9739–9757. doi:10.1002/2015JD023638.Received

887 Schumann, U., Weinzierl, B., Reitebuch, O., Schlager, H., Minikin, a., Forster, C., Baumann, R., Sailer, T., Graf, K.,  
888 Mannstein, H., Voigt, C., Rahm, S., Simmet, R., Scheibe, M., Lichtenstern, M., Stock, P., Rüba, H., Schäuble, D.,  
889 Tafferner, a., Rautenhaus, M., Gerz, T., Ziereis, H., Krautstrunk, M., Mallaun, C., Gayet, J.-F., Lieke, K., Kandler, K.,  
890 Ebert, M., Weinbruch, S., Stohl, a., Gasteiger, J., Groß, S., Freudenthaler, V., Wiegner, M., Ansmann, a., Tesche, M.,  
891 Olafsson, H., Sturm, K., 2011. Airborne observations of the Eyjafjalla volcano ash cloud over Europe during air space  
892 closure in April and May 2010. *Atmos. Chem. Phys.* 11, 2245–2279. doi:10.5194/acp-11-2245-2011

893 Seibert, P., Kristiansen, N.I., Richter, A., Eckhardt, S., Prata, A.J., Stohl, A., 2011. Uncertainties in the inverse modelling of  
894 sulphur dioxide eruption profiles. *Geomatics, Nat. Hazards Risk* 2, 201–216. doi:10.1080/19475705.2011.590533

895 Sofiev, M., 2000. A model for the evaluation of long-term airborne pollution transport at regional and continental scales.  
896 *Atmos. Environ.* 34, 2481–2493. doi:10.1016/S1352-2310(99)00415-X

897 Sofiev, M., Vira, J., Kouznetsov, R., Prank, M., Soares, J., Genikhovich, E., 2015. Construction of an Eulerian atmospheric  
898 dispersion model based on the advection algorithm of M. Galperin : dynamic cores. *Geosci. Model Dev. Discuss.* 8,  
899 2905–2947. doi:10.5194/gmdd-8-2905-2015

900 Spinetti, C., Salerno, G.G., Caltabiano, T., Carboni, E., Clarisse, L., Corradini, S., Grainger, R.G., Hedelt, P.A., Koukouli,  
901 M.E., Merucci, L., Siddans, R., Tampellini, L., Theys, N., Valks, P., Zehner, C., 2014. Volcanic SO<sub>2</sub>SO<sub>2</sub> by UV-TIR  
902 satellite retrievals: validation by using ground-based network at Mt. Etna. *Ann. Geophys. Fast Track.* doi:10.4401/ag-  
903 6641

904 Spivakovsky, C.M., Logan, J.A., Montzka, S.A., Balkanski, Y.J., Foreman-Fowler, M., Jones, D.B.A., Horowitz, L.W.,  
905 Fusco, A.C., Brenninkmeijer, C.A.M., Prather, M.J., Wofsy, S.C., McElroy, M.B., 2000. Three-dimensional  
906 climatological distribution of tropospheric OH: Update and evaluation. *J. Geophys. Res.* 105, 8931–8980.

907 Stohl, A., Prata, A.J., Eckhardt, S., Clarisse, L., Durant, A., Henne, S., Kristiansen, N.I., Minikin, A., Schumann, U., Seibert,  
908 P., Stebel, K., Thomas, H.E., Thorsteinsson, T., Tørseth, K., Weinzierl, B., 2011. Determination of time- and height-  
909 resolved volcanic ash emissions and their use for quantitative ash dispersion modeling: the 2010 Eyjafjallajökull

910 eruption. *Atmos. Chem. Phys.* 11, 4333–4351. doi:10.5194/acp-11-4333-2011

911 Theys, N., Campion, R., Clarisse, L., Brenot, H., van Gent, J., Dils, B., Corradini, S., Merucci, L., Coheur, P.-F., Van  
912 Roozendaal, M., Hurtmans, D., Clerbaux, C., Tait, S., Ferrucci, F., 2013. Volcanic  $\text{SO}_2\text{SO}_2$  fluxes derived from  
913 satellite data: a survey using OMI, GOME-2, IASI and MODIS. *Atmos. Chem. Phys.* 13, 5945–5968.  
914 doi:10.5194/acp-13-5945-2013

915 Thomas, H.E., Prata, A.J., 2011. Sulphur dioxide as a volcanic ash proxy during the April–May 2010 eruption of  
916 Eyjafjallajökull Volcano, Iceland. *Atmos. Chem. Phys.* 11, 6871–6880. doi:10.5194/acp-11-6871-2011

917 Tikhonov, A., 1963. Solution of Incorrectly Formulated Problems and the Regularization Method. *Sov. Math. Dokl.* 5,  
918 1035–1038.

919 Vira, J., Sofiev, M., 2012. On variational data assimilation for estimating the model initial conditions and emission fluxes for  
920 short-term forecasting of SOx concentrations. *Atmos. Environ.* 46, 318–328. doi:10.1016/j.atmosenv.2011.09.066

921 Walker, J.C., Carboni, E., Dudhia, a, Grainger, R.G., 2012. Improved detection of sulphur dioxide in volcanic plumes using  
922 satellite-based hyperspectral infrared measurements: Application to the Eyjafjallajökull 2010 eruption. *J. Geophys.*  
923 *Res. Atmos.* 117, n/a-n/a. doi:10.1029/2011JD016810

924 Wang, J., Park, S., Zeng, J., Ge, C., Yang, K., Cam, S., Krotkov, N., Omar, a. H., 2013. Modeling of 2008 Kasatochi  
925 volcanic sulfate direct radiative forcing: assimilation of OMI  $\text{SO}_2\text{SO}_2$  plume height data and comparison with MODIS  
926 and CALIOP observations. *Atmos. Chem. Phys.* 13, 1895–1912. doi:10.5194/acp-13-1895-2013

927 Wilkins, K.L., Watson, I.M., Kristiansen, N.I., Webster, H.N., Thomson, D.J., Dacre, H.F., Prata, A.J., 2015. Using data  
928 insertion with the NAME model to simulate the 8 May 2010 Eyjafjallajökull volcanic ash cloud. *J. Geophys. Res.*  
929 *Atmos.* 121. doi:10.1002/2015JD023895

930 Winker, D.M., Liu, Z., Omar, A., Tackett, J., Fairlie, D., 2012. CALIOP observations of the transport of ash from the  
931 Eyjafjallajökull volcano in April 2010. *J. Geophys. Res. Atmos.* 117, 1–12. doi:10.1029/2011JD016499

932 Winker, D.M., Vaughan, M.A., Omar, A., Hu, Y., Powell, K.A., Liu, Z., Hunt, W.H., Young, S.A., 2009. Overview of the  
933 CALIPSO mission and CALIOP data processing algorithms. *J. Atmos. Ocean. Technol.* 26, 2310–2323.  
934 doi:10.1175/2009JTECHA1281.1

935 Zehner, C. (Ed.), 2012. Monitoring volcanic ash from space. ESA-EUMETSAT workshop on the 14 April to 23 May 2010  
936 eruption at the Eyjafjöll volcano, South Iceland (ESA/ESRIN, 26-27 May 2010). ESA Publication STM-280.

937

938



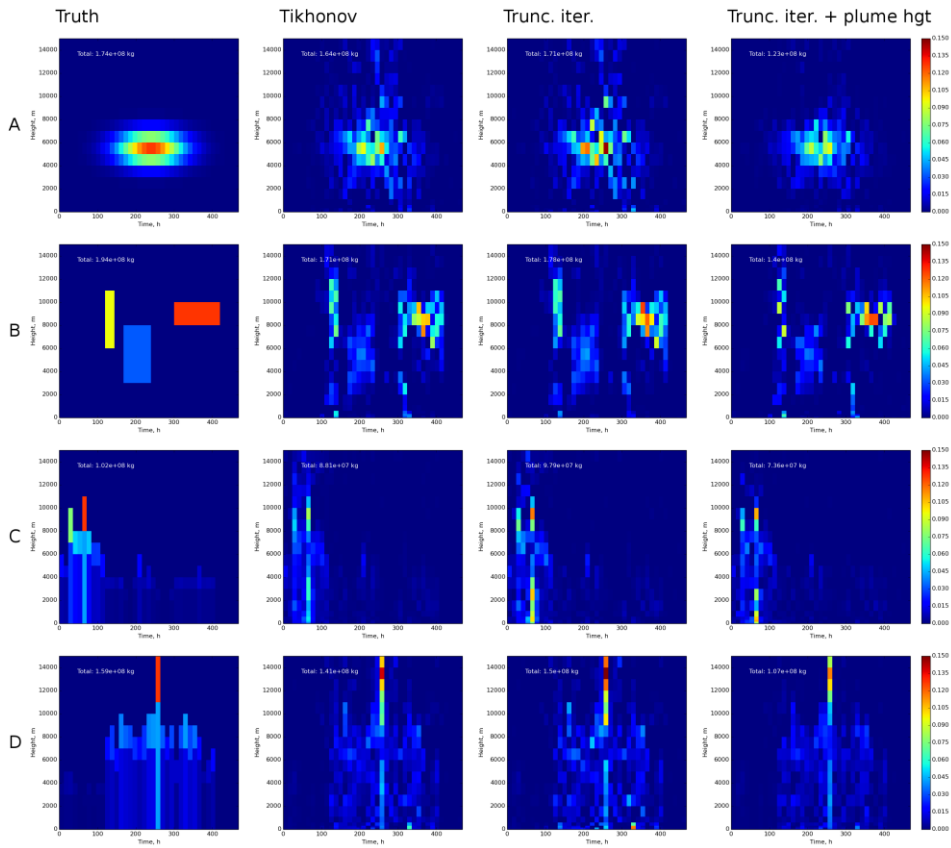
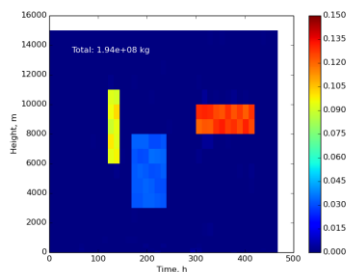


**Figure 14.** Estimated emission flux ( $\text{kg m}^{-1} \text{s}^{-1}$ ) in source term inversions with simulated data. True source terms for the four cases (A to D) are shown in the left column. Solutions using truncated iteration are shown in the middle column, solutions using Tikhonov regularisation are shown in the right column. The remaining columns show the inversion results using Tikhonov regularisation, using truncated iteration with total column data, and using truncated iteration with total column and plume height data.

Formatted: Not Highlight

Formatted: Not Highlight



947 Figure 22. Estimated emission flux with synthetic data: inversion results for the case B in [Figure 1](#) assuming a perfect  
 948 forward model.  
 949

950 Table 1. Bias and RMSE with respect to the true source term (case A...D) in experiments with synthetic data with assimilation of  
 951 total column (TC) and total column and **centre-of-mass plume height** (TC+CM). Values are shown for both optimal regularisation  
 952 (regularisation parameter or iteration number with the lowest RMSE) and for the regularisation chosen from L-curve. Relative  
 953 bias is defined as the difference between estimated and true total emission divided by the true total emission.

Case		Tikhonov regularisation				Truncated iteration			
		RMSE		Relative bias		RMSE		Relative bias	
		Optimal	L-curve	Optimal	L-curve	Optimal	L-curve	Optimal	L-curve
A	TC	48.0	48.0	-5 %	-5 %	45.2	51.2	-3 %	-2 %
	TC+CM	39.8	39.8	-19 %	-19 %	36.5	36.7	-17 %	-17 %
B	TC	65.1	65.6	-8 %	-12 %	61.4	61.9	-8 %	-8 %
	TC+CM	59.3	60.2	-18 %	-23 %	56.9	58.4	-18 %	-17 %
C	TC	21.1	21.1	-13 %	-13 %	20.6	21.9	-8 %	-4 %
	TC+CM	18.5	18.6	-20 %	-24 %	17.8	18.1	-17 %	-17 %
D	TC	32.4	33.6	-15 %	-11 %	31.1	38.0	-8 %	-6 %
	TC+CM	29.3	29.5	-27 %	-24 %	27.3	28.0	-24 %	-21 %

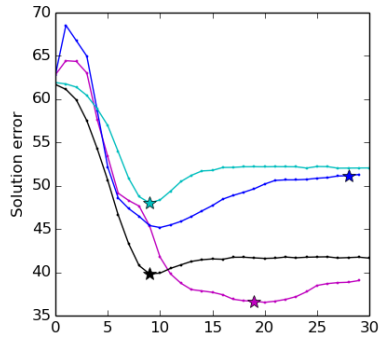
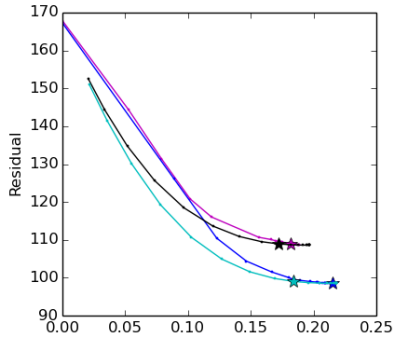
Field Code Changed

Formatted: Not Highlight

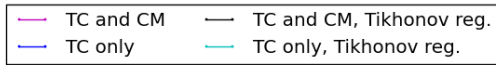
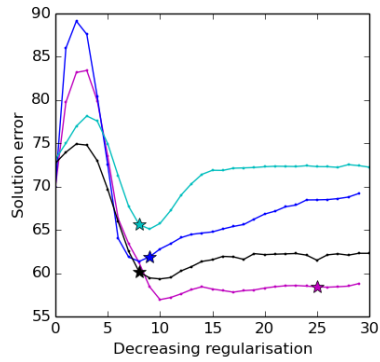
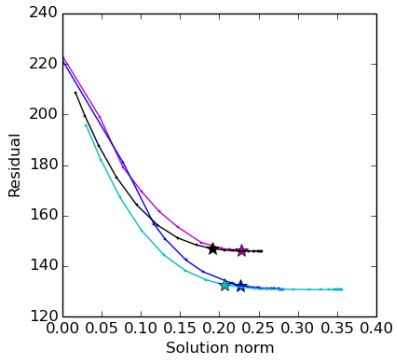
Formatted Table

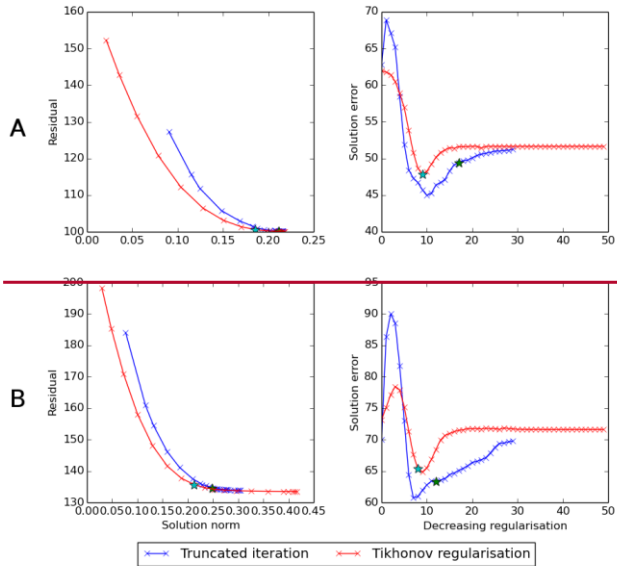
Formatted: Normal

A



B





957

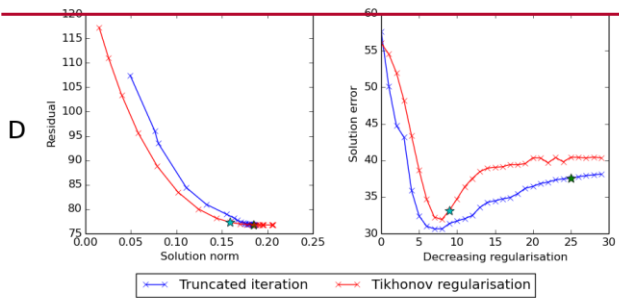
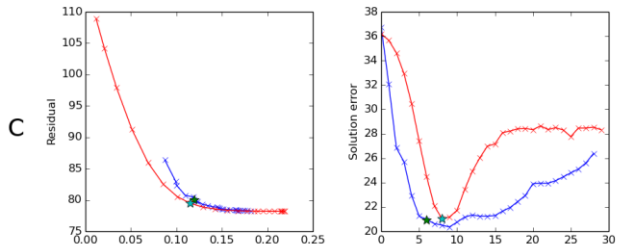
958

959

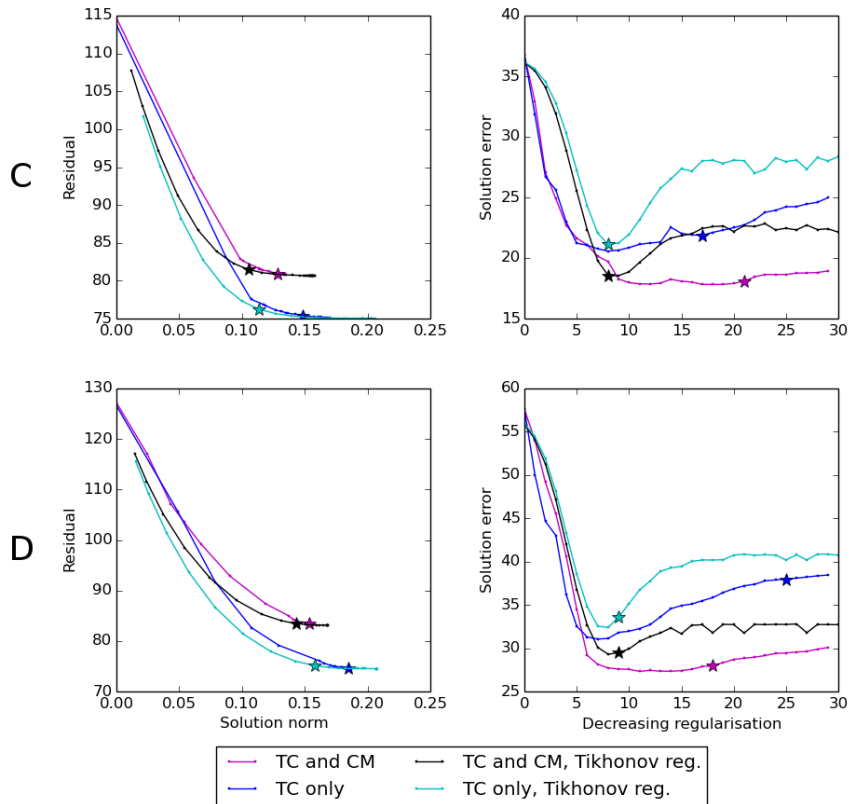
960

Figure 33. L-curve (left) and RMS error (right) for inversions with simulated data for cases A and B in Figure 1. The iterate (for truncated iteration) or the regularisation parameter (for Tikhonov regularisation) chosen from the L-curve is marked with a star.

Formatted: Not Highlight

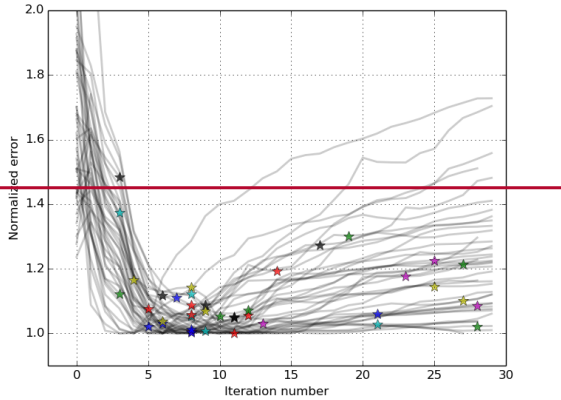


961



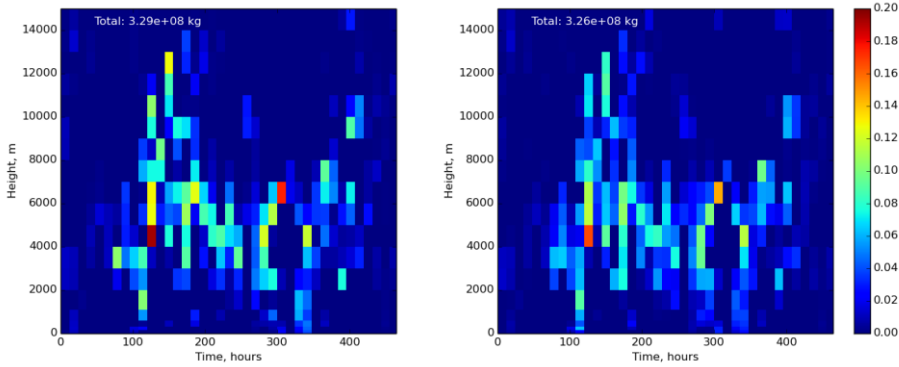
962  
 963 **Figure 44.** L-curve (left) and RMS error (right) for inversions with simulated data for cases C and D in [Figure 1](#). The  
 964 iterate (for truncated iteration) or regularisation parameter (for Tikhonov regularisation) chosen from the L-curve is marked with  
 965 a star.

Formatted: Not Highlight



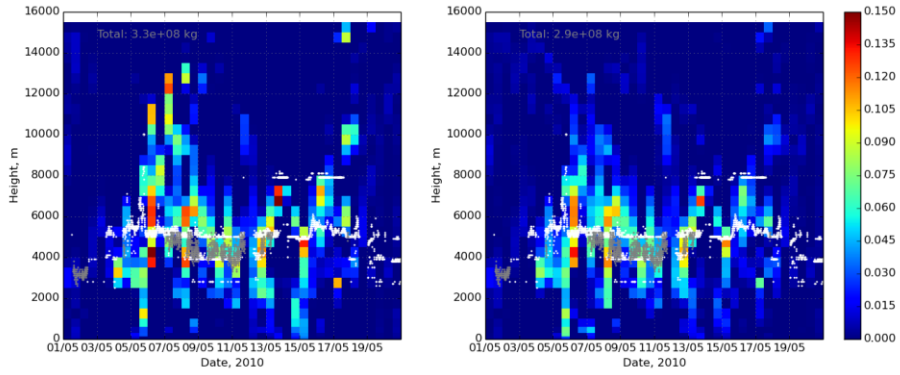
967  
968  
969

Figure 5. The normalised RMSE with respect to iteration number. Each grey line corresponds to an inversion with a randomly generated source term. The colourful stars denote solutions chosen from the L-curve.



970  
971

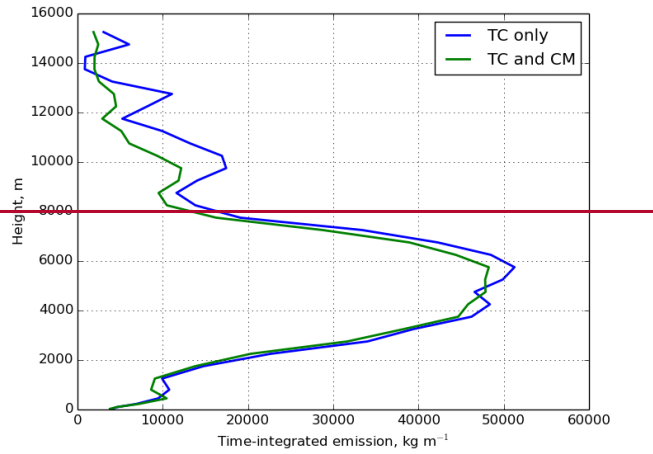
Figure 56. Inversion results with real observations: emission flux ( $\text{kg m}^{-1} \text{s}^{-1}$ ) obtained using 4D-Var (left) and by evaluating the sensitivity matrix (right). The inversions are based on total column observations.



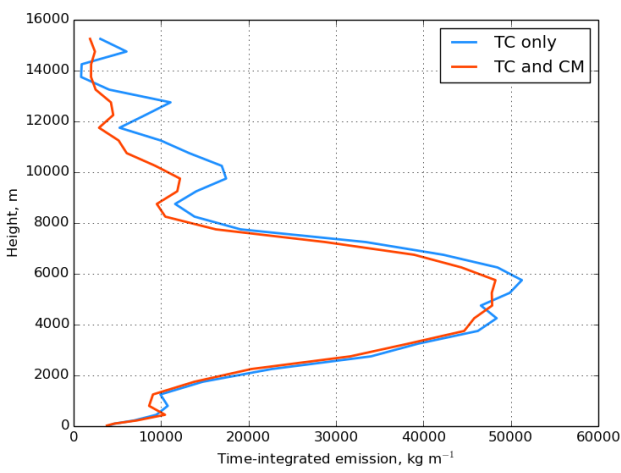
972  
973  
974  
975  
976

**Figure 67.** Inversion results for Eyjafjallajökull. Left: emission flux ( $\text{kg m}^{-1} \text{s}^{-1}$ ) with assimilation of column mass only. Right: assimilation of column mass and plume height with full observation error covariance matrix. White dots denote plume height observations by radar, grey dots denote plume height observations with a camera.





977



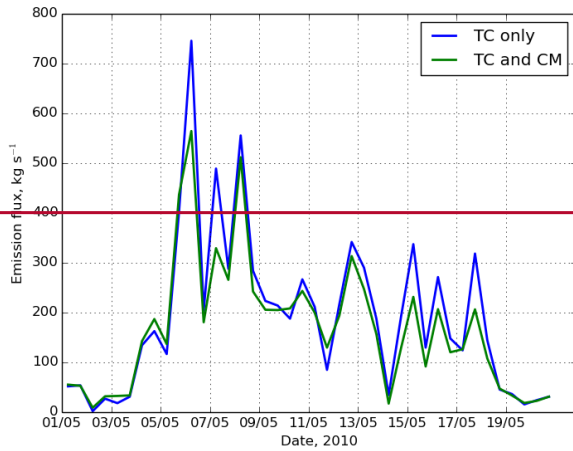
978

979

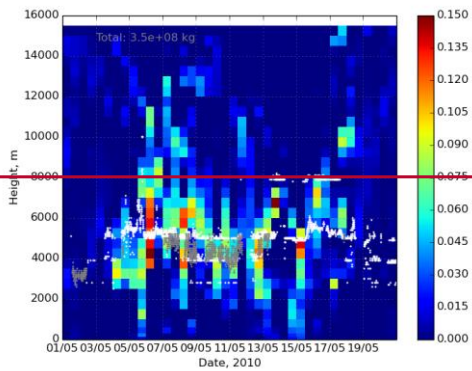
980

Figure 78. Time-integrated emission of  $\text{SO}_2\text{SO}_2$  ( $\text{kg m}^{-1}$ ) during the simulated period as function of height (m) for the source term inversions with (green:red) and without (blue) plume height assimilation.

981



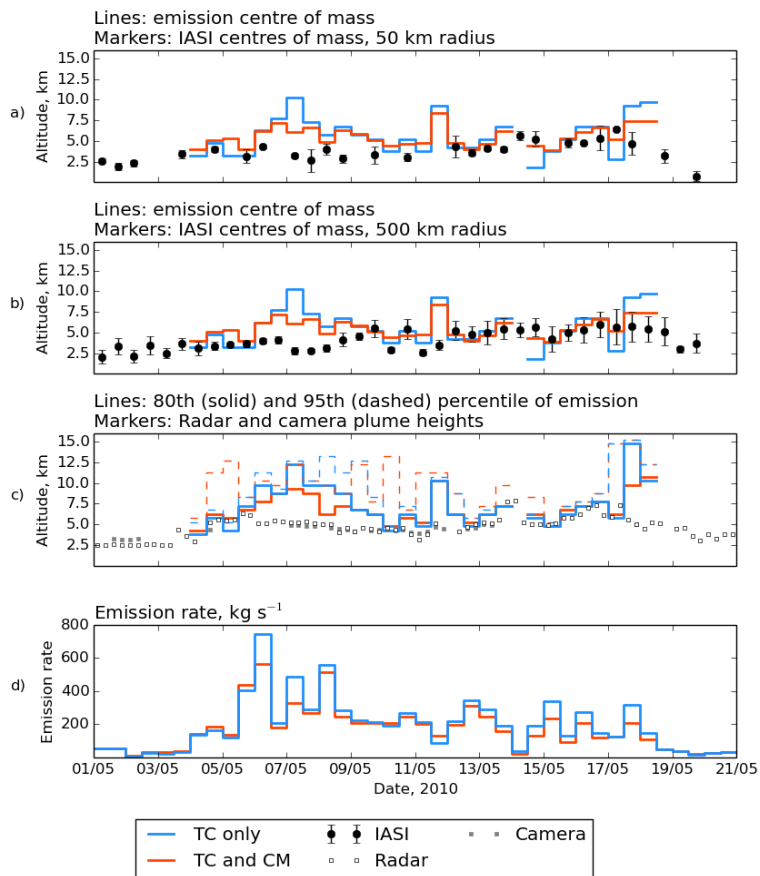
982  
983 **Figure 9. Estimated SO<sub>2</sub> emission flux (kg s<sup>-1</sup>) as function of time with (green) and without (blue) assimilation of plume height**  
984 **retrievals.**



985  
986 **Figure 10. Inversion results for Eyjafjallajökull: emission flux (kg m<sup>-1</sup>s<sup>-1</sup>) with assimilation of column density and plume**  
987 **height but neglecting off diagonal elements in the observation error covariance matrix. White dots denote plume height**  
988 **observations by radar, grey dots denote plume height observations with a camera.**

Formatted: Normal

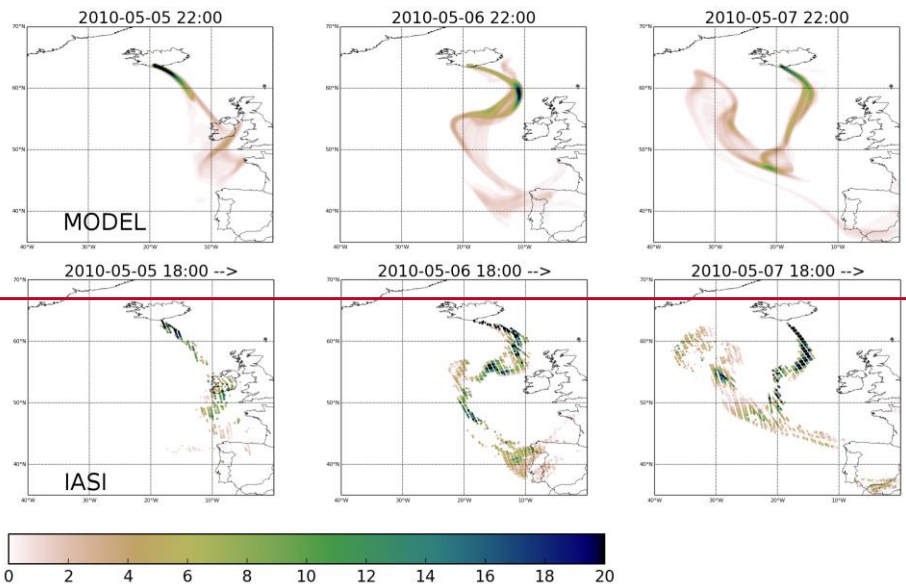
Field Code Changed



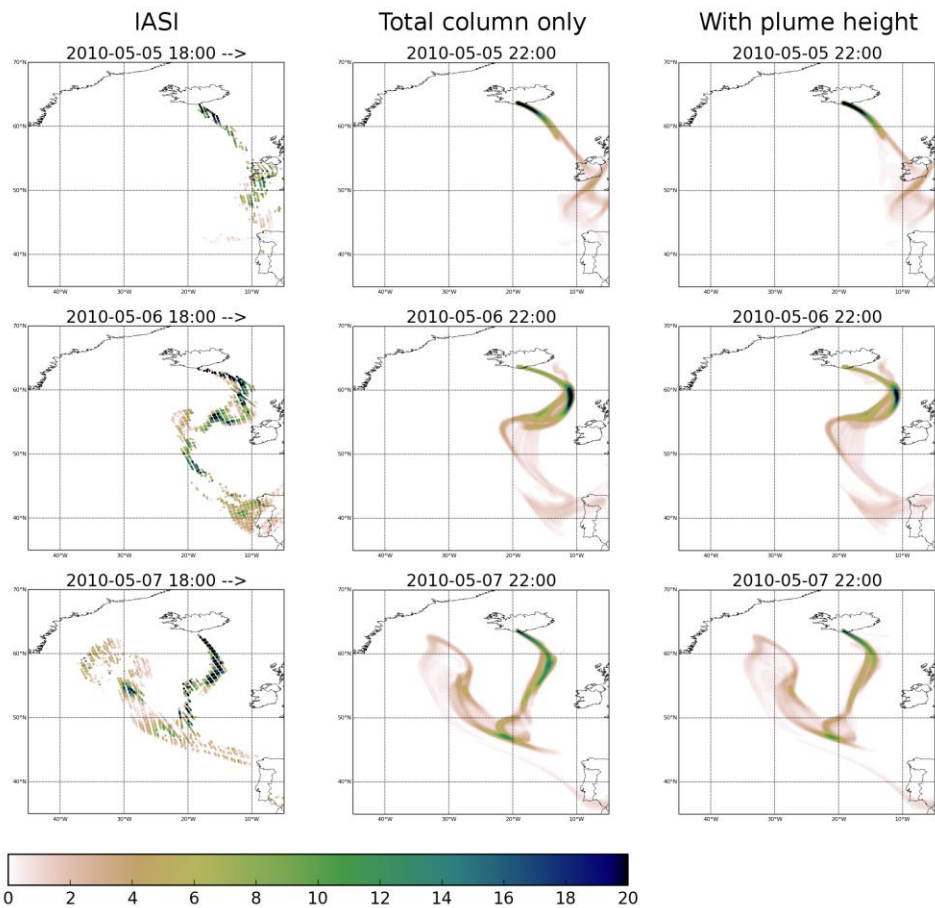
989  
990  
993 **Figure 8. Inversion results for Eyjafjallajökull. Panels a and b: centre of mass of SO<sub>2</sub> injection and average IASI plume height**  
994 **within 50 and 500 km from the volcano; panel c: 95th and 80th percentiles of SO<sub>2</sub> injection and the plume top altitudes observed**  
995 **by radar and camera; panel d: estimated emission rate (kg s<sup>-1</sup>). Inversions using only total column retrievals are plotted in blue;**  
996 **inversions using total column and plume height retrievals are plotted in red. Fully correlated errors are assumed for evaluating**  
997 **the error bars for IASI data. The data with retrieval error estimate larger than 5 km not included. The radar and camera**  
998 **observations are averaged to time steps of 6 hours. The centres of mass and percentiles of the inversion results are evaluated for**  
999 **the 12 hour steps emitting at least 1% of the total emission. All altitudes are above sea level.**  
1000

Formatted: Font: 0 pt, Font color: Black, (none), Character scale: 0%, Border: : (No border), Pattern: Clear (Black)

Formatted: Caption



1001

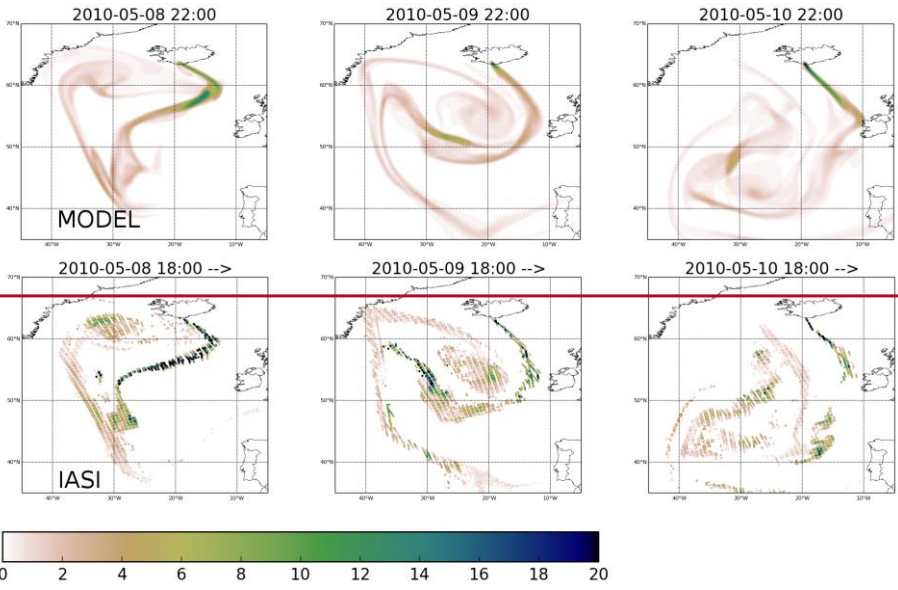


1002  
1003 **Figure 11.** SO<sub>2</sub> column loading (DU) for the a posteriori simulation with assimilation of plume height (top) and for the IASI  
1004 column retrievals (bottom row). Results for 5, 6 and 7th May, 2010 are shown in the columns from left to right. The evening  
1005 overpasses are shown for IASI, the model fields are valid at 22 UTC.

1006  
1007 **Figure 9.** SO<sub>2</sub> column loading (DU) for the IASI column retrievals (left column), for a posteriori simulation with assimilation of  
1008 total column only (middle) and with assimilation of total column and plume height retrievals. Results for 5, 6 and 7th May, 2010  
1009 are shown in the rows from top to bottom. The evening overpasses are shown for IASI, the model fields are valid at 22 UTC.

Formatted: Normal

1011  
1012



1013  
1014

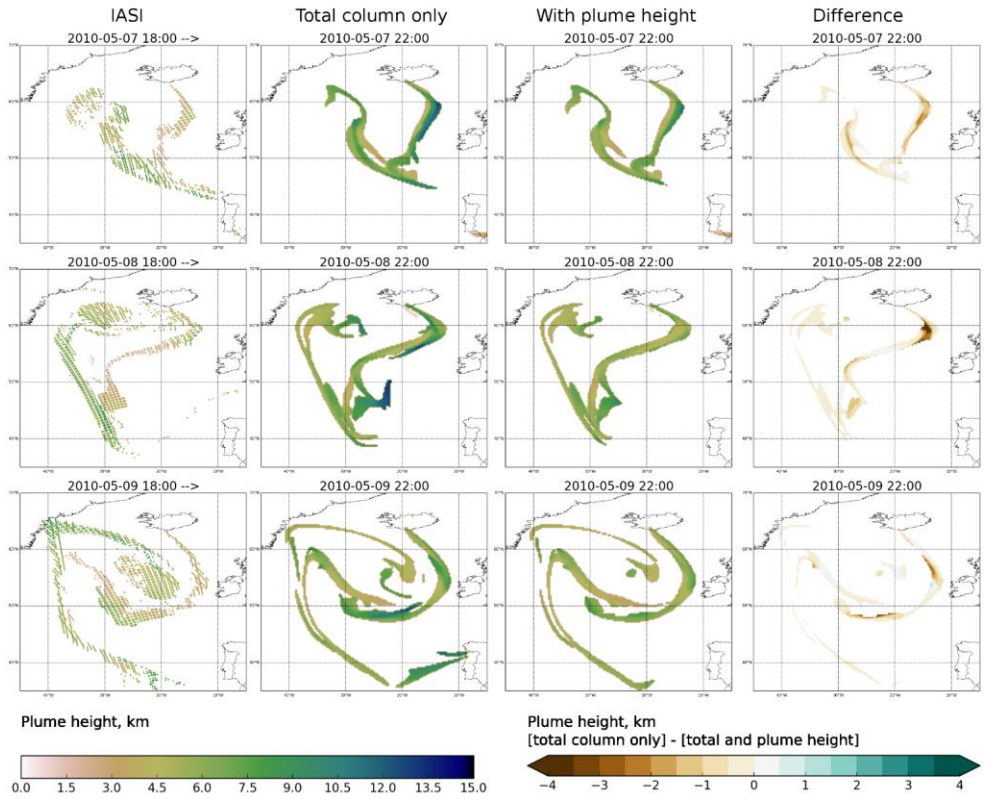
Figure 12. As Figure 11, but 8-10 May, 2010.

Formatted: Normal

Formatted: Indent: First line: 0 cm

Formatted: Normal

1015



1016

1017

1018

1019

**Figure 10. Retrieved SO<sub>2</sub> plume height (km, left column) and the simulated plume height (as centre of mass) without and with assimilation of plume height retrievals for 7-9 (top to bottom row) May, 2010. The difference (without plume height – with plume height) of the simulations is shown in the rightmost column.**

1020

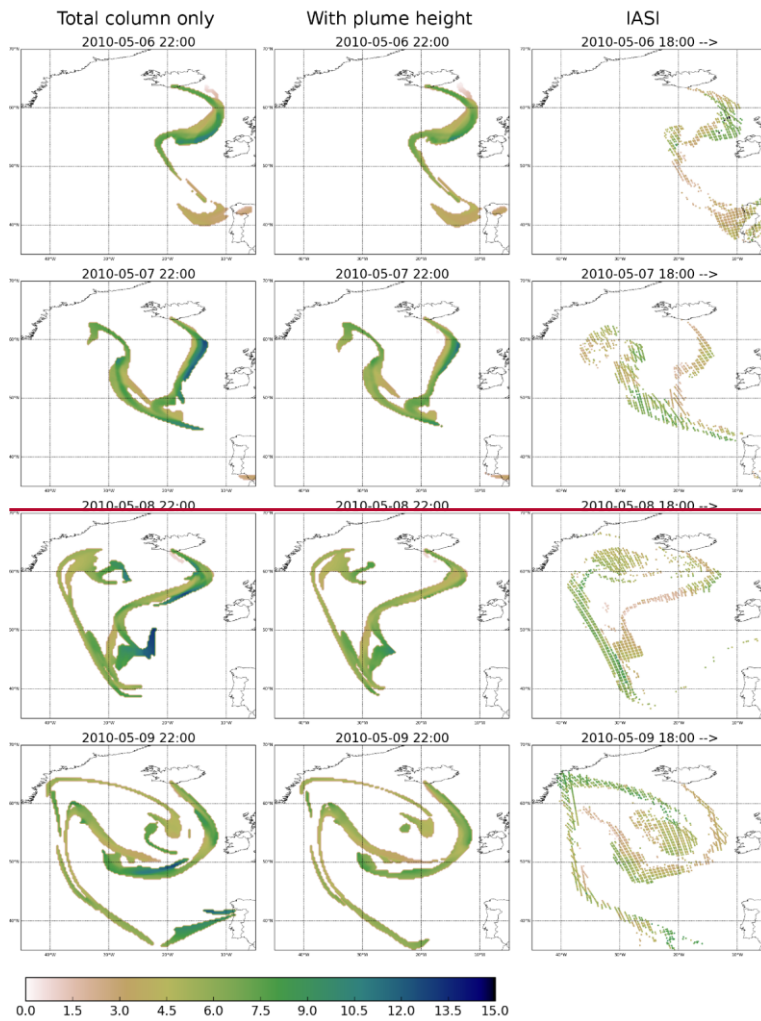
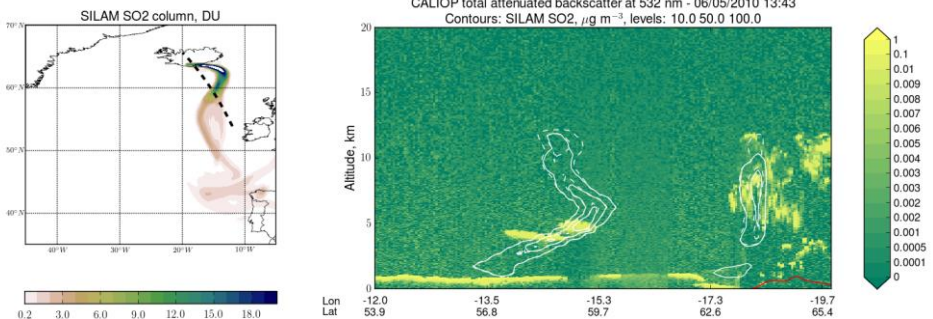


Figure 13. Simulated SO<sub>2</sub> plume height (centre of mass, km) without (left) and with (middle) assimilation of plume height retrievals for 6-9 (top to bottom row) May, 2010. The corresponding IASI retrievals are shown in the right column.

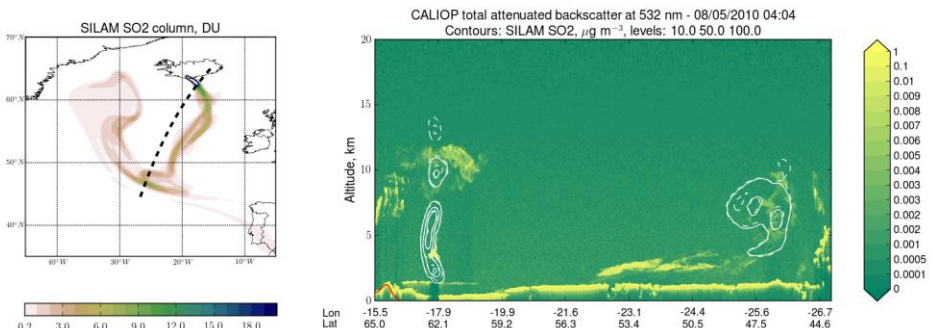
Formatted: Indent: First line: 0 cm



1025  
1026



1027



1028

1029

1030

1031

1032

1033

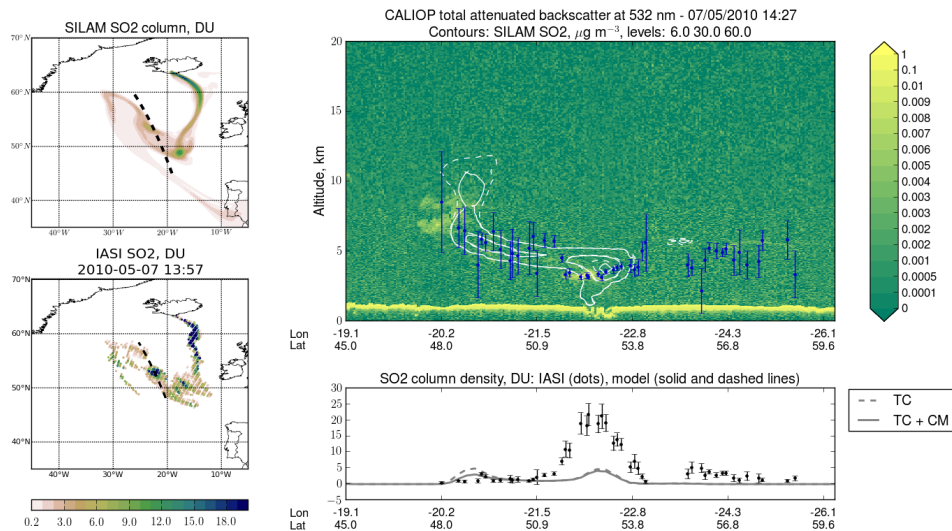
1034

**Figure 11. Comparison of simulated SO<sub>2</sub> with CALIOP data for 14 UTC on 6 May (top) and 04 UTC on 8 May, 2010 (bottom). Left: the simulated SO<sub>2</sub> total column (DU, with assimilation of both total column and plume height) with the CALIPSO track plotted with dashed line. Right: CALIOP total attenuated backscatter at 532 nm with the simulated SO<sub>2</sub> concentration represented by contours. The solid contours correspond to assimilation of both total column and plume height, the dashed contours correspond to assimilation of total column only. The contour levels are 10, 50 and 100  $\mu\text{g m}^{-3}$ .**

Formatted: Indent: First line: 0 cm

Formatted: Caption

1035



1036

1037

1038

1039

1040

1041

1042

1043

**Figure 12. CALIOP total attenuated backscatter, simulated SO<sub>2</sub> concentration (contour levels indicated on the figure title) and collocated IASI plume height retrievals at ~14 UTC on May 7, 2010. The solid lines and contours correspond to inversion using total column and plume height retrievals, dashed lines and contours correspond to inversion using total column retrievals only. The modelled and retrieved column densities are shown in maps on the left and as a 1D plot along the CALIOP track on the bottom. The full CALIOP track segment is marked in the map of simulated SO<sub>2</sub> columns (top-left), the track segment where the collocated IASI data are extracted is shown in the map of retrieved SO<sub>2</sub> columns (bottom-left). The model SO<sub>2</sub> columns shown in the map are from the inversion using both total column and plume height retrievals.**

Formatted: Caption

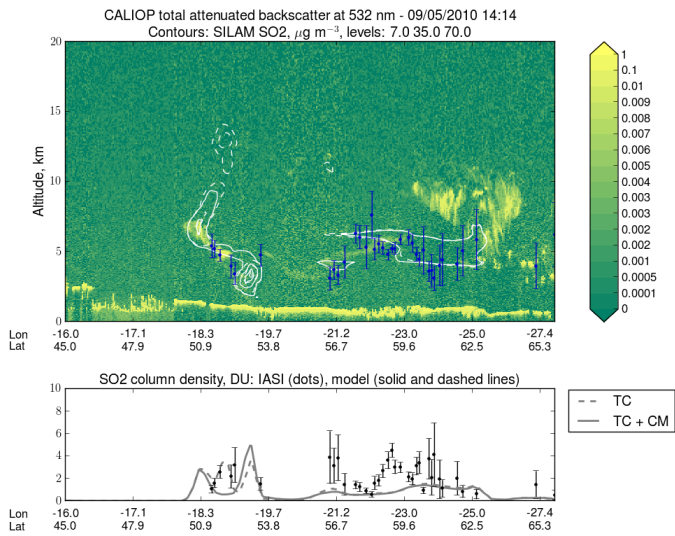
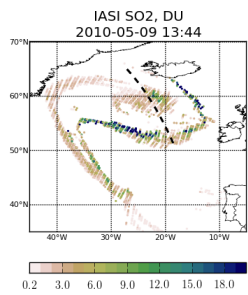
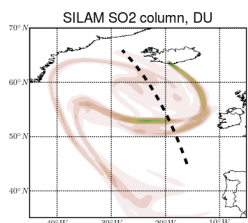


Figure 13. As Figure 12 but for May 9, 2010.

Formatted: Caption

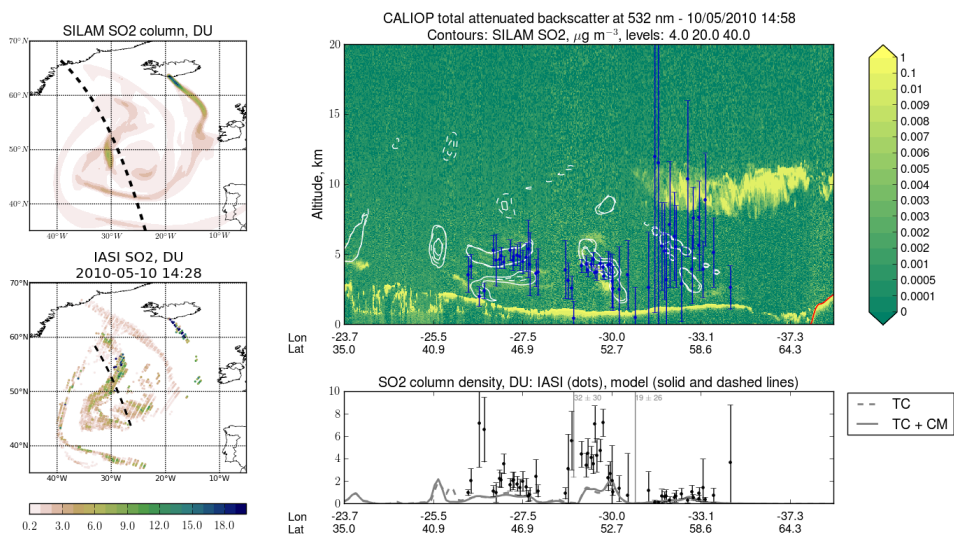


Figure 14. As Figure 12 but for May 10, 2010. In the 1D column density plot below the CALIOP curtain, two IASI data points with values  $32 \pm 30$  and  $19 \pm 26$  DU are outside the plot range.

Formatted: Caption

1046  
1047  
1048